

1 **Hidden vortices: Near-equatorial low-oxygen extremes**
2 **driven by high-baroclinic-mode vortices**

4 Florian Schütte^{1,2}, Johannes Hahn³, Ivy Frenger¹,

5 Arne Bender⁴, Ahmad Fehmi Dilmahamod¹, Marco Schulz¹,

6 Peter Brandt^{1,2}

7
8 ¹GEOMAR Helmholtz Centre for Ocean Research Kiel, Kiel, Germany

9 ²Faculty of Mathematics and Natural Sciences, Kiel University, Kiel,
10 Germany

11 ³Federal Maritime and Hydrographic Agency, Hamburg, Germany

12 ⁴Laboratoire d'Océanographie Physique et Spatiale, University Brest,
13 CNRS, Ifremer, IRD, IUEM, Plouzané, France

14

15 Corresponding Author: Florian Schütte (fschuette@geomar.de)

16

17

18

19

20 **Keywords:** subsurface low-oxygen/hypoxic patches, high-baroclinic
21 mode vortices, subsurface coherent vortices, submesoscale eddies, low-
22 latitudes / tropical / near-equatorial

23 **Abstract**

24 Long-term time series of dissolved oxygen (DO) measurements from the upper 500 m of the
25 eastern tropical North Atlantic (ETNA), collected over a period of up to 15 years at three
26 different mooring sites, reveal recurring extreme low-oxygen events lasting for several weeks.
27 Similarly, observations from 15 individual meridional ship sections between 6°N and 12°N
28 along 23°W show DO concentrations far below 60 $\mu\text{mol kg}^{-1}$ in the upper 200 m - significantly
29 lower than the climatological values in this depth range ($>80 \mu\text{mol kg}^{-1}$). Two-third of these
30 low-oxygen events could be related with high-baroclinic-mode vortices (HBVs) with their cores
31 located well below the mixed layer. Despite the energetic equatorial circulation and the
32 expected dominance of wave-like structures in the near-equatorial region, these HBVs persist
33 as relatively long-lived and coherent features. Based on moored and shipboard observations
34 from the ETNA, and supported by an eddy-resolving ocean-biogeochemistry model, we
35 characterize their dynamics and DO distribution. Observed water mass properties and model
36 analyses suggest that most HBVs originate from the eastern boundary and can persist for
37 more than six months. As they propagate westward into regions of higher potential vorticity
38 (PV), anticyclonic HBVs with low-PV cores remain more effectively isolated and have longer
39 lifespans compared to cyclonic HBVs with high-PV core. The vertical structure of the dominant
40 anticyclonic HBVs corresponds to baroclinic modes 4-10, with associated Rossby radii ranging
41 from 34 km to 13 km, respectively. This is consistent with observed eddy sizes and is well
42 below the corresponding 1st baroclinic Rossby radius of deformation ($> 100 \text{ km}$). Since none
43 of the observed HBVs exhibit a surface signature, a substantial portion of the near-equatorial
44 eddy field may remain undetected by satellites, yet still exert significant influence on local
45 ocean ecosystems and biogeochemical cycles.

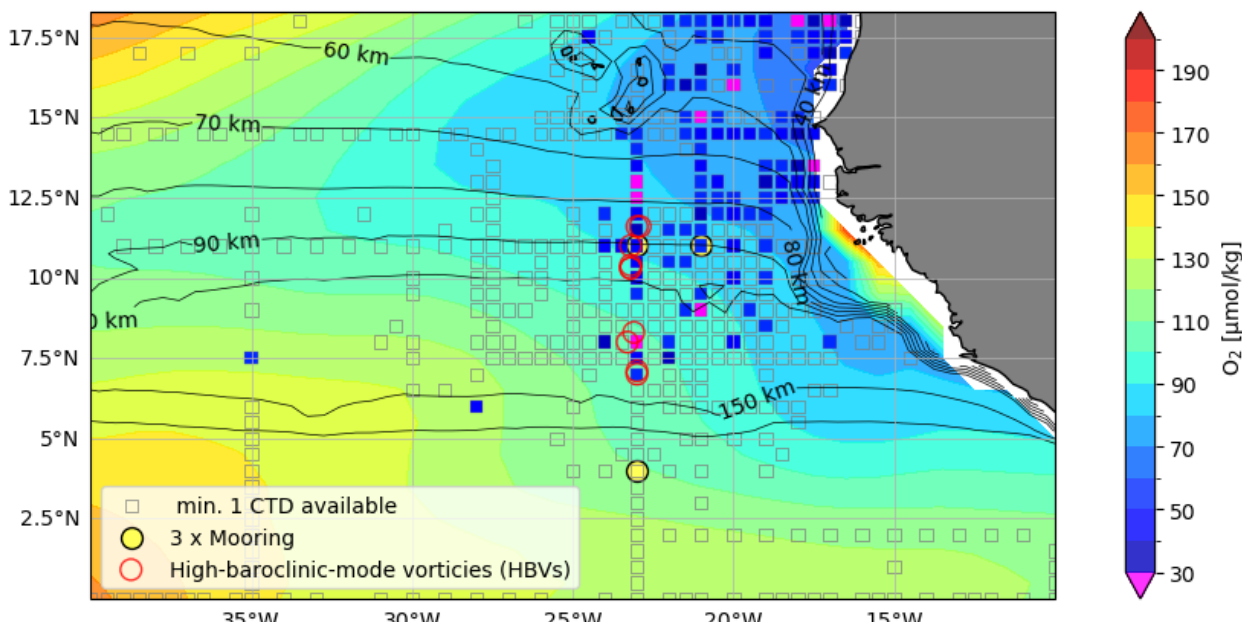
46 **1. Introduction**

47 Dissolved oxygen (DO) concentration is a key component of marine ecosystems, shaping
48 biodiversity, biogeochemical cycles, and the survival of pelagic species (e.g. Deutsch et al.
49 2020). From long-term moored observations in the open Eastern Tropical North Atlantic
50 (ETNA) near the equator (latitudes $<12^{\circ}\text{N}$), we repeatedly observe short-lived extreme low-
51 oxygen events in the subsurface, well below the mixed layer. This DO variability is likely driven
52 by small-scale vortices, which is unexpected, as theory suggests that wave-like structures
53 should dominate at these latitudes (Eden, 2007). In this study, we combine moored time series,
54 repeated ship transects, and an eddy-resolving biogeochemical model to investigate these
55 small-scale processes below the mixed layer in the tropical Atlantic. This integrated approach
56 allows us to characterize their structure, variability, and strong influence on DO distribution,
57 with potential implications for marine ecosystems and biogeochemical cycles.

58 Extreme events of low DO in isolated cores of large coherent mesoscale eddies have become
59 a well-studied phenomenon of the Atlantic and Pacific eastern boundary upwelling systems
60 (e.g. Stramma et al. (2013); Karstensen et al. (2015); Schütte et al. (2016b); Frenger et al.
61 (2018)). A strong isolation and the longevity of such eddies over several months favor the
62 existence of a DO depleted eddy core. The DO depleted core may result from (i) trapped water,
63 which is transported westward within the eddy core from a region of initially low DO, typically
64 from the eastern boundary (dynamic effect) and/or (ii) enhanced DO consumption (production
65 effect) due to a biologically high productive regime above the eddy core (McGillicuddy, 2016).
66 The latter is associated with high phytoplankton productivity, which leads to enhanced
67 respiration and reduction of DO beneath the mixed layer directly in the isolated core reaching
68 down to about 200 m (Karstensen et al., 2017). Respiration rates in the eddy's interior (at
69 around 80m depth) were found to be substantially increased, with up to 3 to 5 times the values
70 of ambient conditions for the tropical North Atlantic (approximately $0.04\text{--}0.06 \mu\text{mol kg}^{-1} \text{d}^{-1}$),
71 e.g. subsurface intensified anticyclonic eddies (subsurface ACEs): $0.19 \pm 0.08 \mu\text{mol kg}^{-1} \text{d}^{-1}$
72 and surface intensified cyclonic eddies (CEs): $0.10 \pm 0.12 \mu\text{mol kg}^{-1} \text{d}^{-1}$ (Schütte et al., 2016b).
73 The increased respiration within these isolated mesoscale eddies may result in anoxic
74 conditions ($< 5 \mu\text{mol kg}^{-1}$) in the otherwise hypoxic ($> 60 \mu\text{mol kg}^{-1}$) ETNA. Such eddies can
75 locally modulate biogeochemical processes and influence marine organisms (Fiedler et al.,
76 2016; Hauss et al., 2016; Löscher et al., 2015). Moreover, it is suggested that the increased
77 DO consumption within the isolated mesoscale eddy cores promote the formation and
78 existence of a broad-scale shallow DO minimum zone (sOMZ) at about 80 m (Schütte et al.,
79 2016b), that is most pronounced off the nutrient-rich Mauritanian upwelling system in the
80 ETNA, located between 15° and 23°N (Karstensen et al., 2008; Brandt et al., 2015) (Fig. 1).
81 For such low DO extremes to develop highly isolated eddies must form and propagate over a

82 relatively long period through regions of relatively low dynamical activity, e.g. as stated in the
83 mentioned literature north of 12°N in the eastern Atlantic and Pacific oceans.

84 The occurrence of DO depleted long-lived coherent eddies in near-equatorial waters (< 12°) is
85 not intuitive and contrasts theoretical considerations of equatorial dynamics, which suggest a
86 dominance of anisotropic wave like structures (Eden, 2007). However, several extreme low
87 DO events have been observed in the ETNA at latitudes between 6° and 12°N (Brandt et al.
88 2015), where Christiansen et al. (2018) associated one of these events (at 8°N, 23°W) with a
89 subsurface ACE. These eddies are expected to be less isolated and shorter-lived compared
90 to eddies poleward of these low latitudes. The first baroclinic Rossby radius of deformation
91 ($R_{d,1}$), which is a characteristic threshold size of a dynamical regime to be in a geostrophic
92 balance on meso- and larger scales, strongly increases towards the equator (Chelton et al.,
93 1998). Global eddy studies, mainly based on altimeter sea surface height data, show a strong
94 equatorward decrease of long-lived (> 35 days) eddies (Chaigneau et al., 2009; Chelton et al.,
95 2011). Less isolated eddies more readily entrain DO from surrounding waters, while short-lived
96 eddies do not persist long enough to substantially deplete DO in their cores. Both factors inhibit
97 the development of a low DO extreme within eddy cores. Additionally, the equatorial region -
98 compared to the eastern parts of the oceans north of 12°N - is highly dynamic. It features the
99 energetic equatorial zonal current system with associated instabilities as well as various wave
100 phenomena (e.g. Urbano et al. 2006; Brandt et al. 2015; Pena-Izquierdo et al., 2015; Calil et al.,
101 2023; Köhn et al. 2024). Nevertheless, our observations occasionally reveal DO values
102 significantly below the climatological value (Fig. 1).



103
104 Figure 1: Map of the eastern tropical North Atlantic. Shaded are minimum DO values in the

105 upper 200 m of the climatological DO distribution from the World Ocean Atlas 2023. The small
106 squared boxes indicate regions of 0.5 degree boxes for which at least one CTD station is
107 available. These boxes are colored with their minimum DO concentration in the upper 200m
108 (from multiple CTDs, if available) only if the minimum DO concentration is less than 60 $\mu\text{mol/kg}$.
109 Red circles suggest the occurrence of high-baroclinic mode vortices as analyzed in detail in
110 the manuscript. The yellow points mark the positions of the moorings analyzed in the
111 manuscript. The black contour indicates the first baroclinic Rossby radius of the deformation
112 (in km), calculated from the World Ocean Atlas data, following Chelton et al., (1998).

113

114 While mesoscale eddies of the first baroclinic mode can hardly exist at near-equatorial
115 latitudes, smaller-scale eddies might. In the following, we refer to these smaller eddies, which
116 still exhibit similar dynamics to mesoscale eddies - i.e., they are dominantly in geostrophic
117 balance – as high-baroclinic mode vortices (HBVs). They have radii below the first baroclinic
118 Rossby radius, $R_{d,1}$, and baroclinic modes larger than one (D'Asaro, 1988; McCoy et al., 2020,
119 McWilliams et al 1985, 2016). These HBVs, often referred to in the literature as subsurface or
120 submesoscale coherent vortices, are observed to have isolated cores and can therefore advect
121 tracers (Gula et al., 2019). Due to their small spatial scales and since they often appear at
122 subsurface depth, these eddies are not necessarily detectable from satellite observations
123 (McCoy et al., 2020). HBVs are not typically known to persist for extended durations in near-
124 equatorial waters. However, here we provide evidence that HBVs may serve as a potential
125 mechanism driving the observed low-oxygen extremes at these low latitudes. When linked to
126 biogeochemical anomalies, HBVs may play a role in shaping local biogeochemical conditions
127 and ecosystem variability. However, ocean models are often submesoscale “permitting” only,
128 in the sense that the model has sufficient resolution to begin representing submesoscale
129 processes but does not fully resolve them, particularly with increasing distance from the
130 equator. Understanding the frequency and behavior of HBVs is essential for understanding
131 tracer distributions, developing effective parameterizations and improving model accuracy.

132 In this study, we identify the characteristics, origin and temporal evolution of low-oxygen
133 extremes in the upper 200 m of the tropical Atlantic Ocean and discuss the role of HBVs in
134 driving these DO deficient zones. We use a comprehensive dataset of in situ moored and
135 shipboard observations combined with an actively eddying ocean-biogeochemistry model
136 (respective data and methods introduced in *section 2* and *3*) in order to investigate the
137 frequency distribution and magnitude of these events (*section 4.1*). We show that the low-
138 oxygen events are mostly associated with subsurface intensified HBVs (*section 4.2*), both
139 anticyclonic and cyclonic. We derive the demography of these structures from an eddy
140 detection algorithm applied to in-situ observations (*section 4.3*) and a vertical baroclinic mode
141 analysis (*section 4.4*). The core water of the HBVs is analysed in *section 4.5* and the origin
142 and temporal evolution of the HBVs based in model simulations is shown in *section 4.6*. We

143 give a detailed discussion in *section 5* and provide a summary in *section 6*.

144

145 **2. Data**

146 Data from moored, shipboard and satellite observations, climatological data as well as the
147 output of an actively eddying ocean-biogeochemistry model from the tropical North Atlantic
148 were used within this study as described in the following.

149 **2.1. Moored observations**

150 Multi-year moored observations from three different locations 11°N/21°W; 11°N/23°W and
151 4°N/23°W were used in this manuscript (Fig. 1). The mooring at 11°N/21°W was equipped with
152 DO (AADI Aanderaa optodes of model types 3830 and 4330) and CTD (Conductivity,
153 temperature, depth) sensors (Sea-Bird SBE37 microcats) which were attached next to each
154 other on the mooring cable between 2012 to 2018. Eight of these optode/microcat
155 combinations were installed evenly distributed in the depth range between 100 to 800 m,
156 delivering multi-year time series of temperature, salinity and DO with a temporal resolution of
157 up to 5 min. At 800 m depth, an upward looking Acoustic Doppler Current Profiler (ADCP) was
158 installed to record velocity in the depth range between about 60 and 800 m. During the 2nd
159 deployment period (May 2014 to Sep 2015), no velocity observations were available due to a
160 failure of the ADCP. Before and after a deployment period, optodes and microcats were
161 calibrated against CTD-O measurements during CTD casts and onboard lab measurements
162 as described in Hahn et al. (2014) and Hahn et al. (2017). The correction against reference
163 measurements, thereby considering potential sensor drifts (Bittig et al., 2018), allowed best
164 data quality and yielded average root mean square calibration errors of 0.003°C, 0.006 and
165 3 µmol kg⁻¹ for temperature, salinity and DO, respectively. Only quality controlled data that
166 was flagged good was used for further analysis. ADCP measurements were quality controlled
167 against a percent good criterion (20% threshold) and were checked for plausibility and evident
168 outliers due to surface reflection. ADCP bin depths were corrected using a mean sound speed
169 profile following the approach by Shcherbina et al. (2005). This mooring is used to study
170 hydrographic, DO and velocity temporal variability (on daily to intraseasonal time scales)
171 related to low-oxygen extreme events. The other moorings at 11°N/23°W and 4°N/23°W are
172 part of the prediction and research moored array in the tropical Atlantic (PIRATA), which were
173 equipped with DO (AADI Aanderaa optodes of model types 3830 and 4330) sensors at 300 m
174 and 500 m depth from 2009 to 2024. At 11°N/23°W additionally a DO sensor at 80 m depth

175 was installed between 2017 to 2024. The DO sensors deliver hourly data and are calibrated
176 and processed in the same way as described above.

177 **2.2. Shipboard observations**

178 Hydrographic and DO data was obtained from CTD-O casts, that were carried out during a
179 large number of research cruises to the tropical North Atlantic between 2006 and 2022. In the
180 region 6°-12°N and 30°-18°W, 976 profiles were recorded during 24 cruises mainly covering
181 the upper 1300 m of the water column. Two independently working systems of temperature-
182 conductivity-pressure-oxygen sensors were used, that allowed to identify spurious sensor
183 data. Salinity and DO readings were calibrated against values from water samples, that were
184 taken during the majority of CTD-O profiles of each individual cruise and that were measured
185 onboard with salinometry and Winkler titration, respectively. For a single cruise, data accuracy
186 was generally better than 0.002°C, 0.002 and 2 µmol kg for temperature, salinity and DO,
187 respectively.

188 The majority of research cruises covered the 23°W meridian in the tropical North Atlantic. They
189 captured several low-oxygen extreme events in the latitude range between 6° and 12°N (Fig.
190 1). We made use of these CTD-O observations that were mostly carried out at a meridional
191 resolution of 0.5°, corresponding to 55 km, in order to investigate the spatial distribution of the
192 low oxygen extremes. Horizontal velocity data were additionally acquired continuously along
193 the cruise track with vessel-mounted Acoustic Doppler Current profilers (vmADCPs). The
194 typical vmADCP operating frequency was 75 kHz, where 1-hour averaged data has an
195 accuracy of better than 2-4 cm s⁻¹ (Fischer et al., 2003). During one cruise, a vmADCP system
196 with 150 kHz operating frequency was used and we expanded this data set with data from a
197 lowered ADCP (IADCP), that was attached to the CTD rosette and measured velocity profiles
198 at CTD-O cast positions. Single velocity profiles from IADCP had an accuracy of better than
199 5 cm s⁻¹ (Visbeck, 2002). The horizontal velocity observations from all 23°W ship sections
200 covered the depth range of the upper 300 m, the depth where the extreme low-oxygen occur
201 and thus coinciding with our target depth range.

202 For each 23°W ship section hydrography, DO and velocity were mapped onto a regular depth-
203 latitude grid (resolution of 10 m and 0.05°) using a Gaussian interpolation scheme with vertical
204 and horizontal influence (cutoff) radii of 10 m (20 m) and 0.05° (0.1°), respectively (for details
205 see Brandt et al. (2010). This is done to plot the average section along 23°W in order to
206 compare it with the model data and assess the model performance.

207 **2.3. Satellite observations**

208 Sea level anomaly (SLA) and surface geostrophic velocity derived from satellite altimetry
209 products were used in this study to identify the surface signatures of eddies. The multimission
210 Data Unification and Altimeter Combination System (DUACS) product in delayed time and

211 daily resolution with all satellite missions available at a given time is used. It has a spatial
212 resolution of 0.25° and is provided by Marine Copernicus (<https://doi.org/10.48670/moi-00148>).

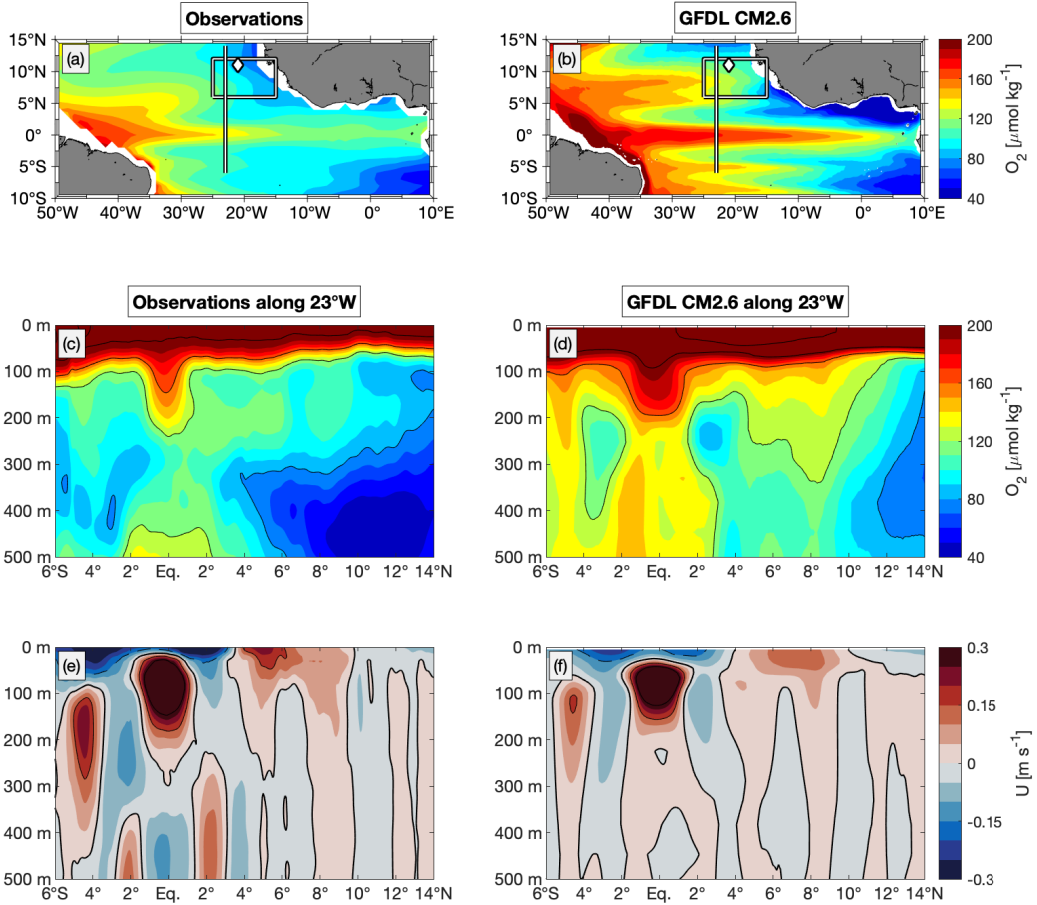
214 **2.4. Climatological data**

215 Gridded climatological hydrography and DO from the World Ocean Atlas 2023 (WOA23)
216 (described e.g. in Reagan et al. 2024) was used as a reference data set throughout this study.
217 For more details see section 6 *Data availability*.

218 **2.5. Coupled ocean-biogeochemistry model**

219 We used the output of the GFDL climate model with an eddy-rich ocean, CM2.6 (Delworth et
220 al., 2012; Griffies et al., 2015) to further understand the origin and development of low-oxygen
221 extremes in the tropical ocean. CM2.6 has a nominal ocean resolution of 0.1 degrees and an
222 atmosphere with approximately 50 km resolution. For computational efficiency, marine
223 biogeochemistry is represented by the simple biogeochemical model MiniBLING (Galbraith et
224 al., 2015). MiniBLING was run with the three prognostic tracers dissolved inorganic carbon,
225 phosphate and DO. Organic carbon (biomass) is treated diagnostically and is not advected in
226 the model. Despite its simplicity, MiniBLING has been shown to perform comparably well to
227 more complex marine biogeochemical models in simulating marine biogeochemistry and its
228 sensitivity to climate (Galbraith et al., 2015). Moreover, the small number of tracers was not
229 just a limitation but a key factor that made it possible to run a simulation with a mesoscale-rich
230 ocean.

231 The results we show here stem from a simulation with preindustrial atmospheric carbon dioxide
232 levels that has been run for 200 years, with marine biogeochemistry coupled at year 48. The
233 model has been spun up from rest with initial conditions from WOA09 (Locarnini et al., 2010;
234 Antonov et al., 2010; Garcia et al., 2010a; Garcia et al., 2010b) and Global Ocean Data
235 Analysis Project (GLODAP) (Key et al., 2004). For more details on the model set up and a
236 general evaluation of the model we refer to Griffies et al. (2015) and Dufour et al. (2015). Here,
237 we used model output averaged over five-day intervals for the last 20 years of the simulation.
238 A brief evaluation of the model performance for the northern hemispheric Atlantic DO
239 conditions, the focus of our study, is given in the following.



240

241 Figure 2: Observation-model comparison of the minimum DO between 0 and 200 m of the
 242 time-average distribution from (a) the World Ocean Atlas 2023 and (b) from last 20 years of
 243 GFDL CM2.6 model. Latitude-depth section, 0-500 m along 23°W, of mean DO from (c) repeat
 244 ship sections and (d) last 20 years of GFDL CM2.6 model. (e) and (f) are similar to (c) and (d),
 245 but mean zonal velocity is shown. The box in (a) and (b) illustrates the area of interest in this
 246 study; the line denotes the 23°W section that is shown in subpanels (c) to (f). This section has
 247 been surveyed by 15 individual shipboard observations that are used in this study for the
 248 latitude range 6°N-12°N. Diamond marks the mooring position (11°N/21°W), where data used
 249 in this study were taken.

250 The distribution of the minimum DO between 0 and 200 m taken from the time averaged over
 251 the last 20 years of the GFDL CM2.6 model output (Fig. 2b), shows similar large-scale patterns
 252 as the same corresponding distribution taken from the World Ocean Atlas 2023 climatology
 253 (Fig. 2a): well oxygenated western boundary region, decreasing DO values toward east with
 254 off-equatorial OMZs on both sides of the equator showing minimal values at the eastern
 255 boundary. The simulated distribution has higher DO concentration at the western boundary
 256 and in the interior basin, and partly lower values at the eastern boundary compared to the
 257 climatological distribution from observations, which is particularly the case in the Gulf of Guinea
 258 region. In the interior basin, meridionally alternating bands of oxygen-poor and oxygen-rich
 259 water, that are associated with shallow east- and westward current bands, are pronounced in
 260 GFDL CM2.6, albeit more intensified.

261 In the ETNA, the average DO distribution along 23°W in GFDL CM2.6 (Fig. 2d) shows a
262 notable mismatch with observations (Fig. 2c). While observations from repeat ship sections
263 reveal two distinct OMZ layers - a shallow OMZ above 200 m and a deeper OMZ at 300 - 700
264 m - the model instead simulates only a single OMZ spanning 100 - 600 m. This bias is also
265 present in other coupled ocean circulation biogeochemistry models (e.g. Duteil et al., 2014)
266 and can be attributed, among other factors, to the limited representation of physical transport
267 processes such as submesoscale eddies, which locally enhance oxygen minima. Additionally,
268 simplified or parameterized remineralization and biological processes fail to reproduce rapid
269 upper-ocean oxygen consumption. These discrepancies highlight the importance of direct
270 observational studies, such as ours, which provide detailed insights into the shallow oxygen
271 minimum and its connection to low-oxygen events and high-baroclinic vortices, thereby
272 motivating the focus of this study.

273 Further differences appear south of the equator, where the observed OMZ is absent in the
274 model along 23°W. Instead, GFDL CM2.6 simulates lower DO levels between 2°- 4°N at
275 depths below 150 m compared to observations. The corresponding section of zonal velocity
276 (Fig. 2f) indicates that the model represents upper-ocean currents (above 200 m) well when
277 compared to observations (Fig. 2e). However, below 200 m in the equatorial region (5°S -5°N),
278 zonal currents are considerably weaker and partly misrepresented. North of 5°N, the velocity
279 structure is generally better captured.

280 Despite differences in spatial details and magnitudes the basic features of the DO and velocity
281 distributions are in the upper 200 m of the ETNA, and the GFDL CM2.6 model provides a
282 robust physical and biogeochemical background state to study the role of eddies in driving
283 local DO deficient zones. With a nominal ocean resolution of 0.1°, CM2.6 is mesoscale eddy-
284 resolving and submesoscale-permitting at low latitudes, capturing only the larger
285 submesoscale vortices. The local Rossby radius of deformation (60–150 km; Fig. 1) in the area
286 is resolved, but smaller eddies are near the lower limit of resolvable scales. However, the
287 model has been shown to simulate low-oxygen mesoscale eddies at latitudes poleward of
288 about 12° latitude (Frenger et al., 2018) and provides as a useful framework in this study to
289 complement the observational analysis. Here, we use the last 20 years of this model run to
290 study low-oxygen extreme events in the ETNA equatorward of 12°N.

291 3. Methods

292 Different diagnostics have been applied in this study, that allowed us to associate low-oxygen
293 features with HBVs and to analyze their origin and temporal evolution. The concept of vertical
294 baroclinic modes (*section 3.1*) was used to characterize the vertical structure of HBVs, to

295 identify the dominant vertical modes, and their associated Rossby radius of deformation and
296 propagation speed. In *section 3.2*, we briefly present the calculation of PV, which is used as a
297 conservative tracer to track and to identify the isolation of different water masses. In *section*
298 *3.3*, we describe the different approaches for eddy identification from shipboard observations
299 and in the GFDL CM2.6 model.

300 **3.1. Vertical baroclinic modes and Rossby radius of deformation**

301 A powerful way to describe linear wave dynamics in the ocean is the decomposition into vertical
302 baroclinic modes (Philander, 1978). Each baroclinic mode is associated with a specific gravity
303 wave speed and a corresponding Rossby radius of deformation, which defines its
304 characteristic horizontal length scale.

305 **3.1.1. Baroclinic mode decomposition**

306 The concept of baroclinic modes is based on the linearized hydrostatic equations of motion,
307 which can be separated into a horizontal and a vertical component. Assuming a motionless
308 background state and a flat-bottomed ocean, the vertical structures are given by solving the
309 eigenvalue problems (Gill, 1982):

$$\frac{d^2\Psi_n(z)}{dz^2} + \frac{N^2(z)}{c_n^2} \Psi_n(z) = 0 \quad (1)$$

310 where $\Psi_n(z)$ describes the vertical structures of isopycnal displacement ξ or vertical velocity
311 w and z is the vertical coordinate. $N(z)$ is the vertical profile of the Brunt-Väisälä frequency
312 and c_n the gravity wave speed for mode $n \in \mathbb{N}$. For the eigenvalue problem (1), we use
313 boundary conditions with a free surface and a flat bottom (Gill, 1982), which are given as
314

$$\Psi_n = \frac{c_n^2}{g} \frac{d\Psi_n}{dz}, \text{ at } z = 0 \quad \text{and} \quad \Psi_n = 0, \text{ at } z = -H \quad (2)$$

315 where H is the ocean depth and g the gravitational acceleration. For a continuously stratified
316 ocean, the number of solutions depends on the vertical resolution of the data used. Any
317 perturbances can be described as a superposition of orthogonal vertical baroclinic modes ($n =$
318 $1, 2, 3, \dots$). Amplitudes of vertical structure functions are normalized such that

$$\int_{-H}^0 \Psi_n \Psi_m dz = \delta_{nm} H$$

320 where δ_{nm} is the Kronecker delta and n, m the modes. The gravity wave speed is related to
321 the Rossby radius of deformation, that can be calculated for the off-equatorial regions
322 (poleward of 5°S and 5°N) as

323

$$R_{d,n} = \frac{c_n}{|f|} \quad (3)$$

324 (Gill, 1982 or Chelton, 1998), where $R_{d,n}$ is the Rossby radius of deformation for the n -th
325 vertical baroclinic mode, and f is the Coriolis parameter.

326 **3.1.2. Calculation of vertical baroclinic modes and modal decomposition**

327 The main goal is to decompose any disturbed state into the set of orthogonal baroclinic modes
328 that solve (1). Each hydrographic profile from an individual CTD-O profile can be considered
329 as a perturbation from the mean state. The mean state distribution was derived from the 3-D
330 climatological hydrographic field (cf. Chelton et al. (1998)) that is given by the World Ocean
331 Atlas (section 2.4). Given the corresponding density profile, we calculated the isopycnal
332 displacement $\xi(z)$ by

$$\xi(z) = \frac{\rho'(z) \cdot g}{\rho_0 \cdot N^2} \quad (4)$$

333 with $\rho'(z) = \rho(z) - \rho_{ref}(z)$, $\rho_0 = 1025 \text{ kg/m}^3$ a constant reference density and ρ_{ref} being the
334 undisturbed profile of potential density (here taken as the climatological density profile from
335 the World Ocean Atlas – see also Vic et al. 2021 for more details on the method used). The
336 isopycnal displacement of the disturbed state can be described as a superposition of the
337 orthogonal set of vertical baroclinic modes for displacement, i.e.

$$\xi(z) = \sum_{n=1}^K x_n \Psi_n(z) \quad (5)$$

338 Here, $K \rightarrow \infty$ expresses the exact solution with an infinite number of vertical modes for a
339 continuously stratified ocean. The expansion coefficients x_n are the modal amplitudes. The
340 modal amplitudes are obtained by projecting the observed fields onto the structure functions

341 computed from the World Ocean Atlas. The projection is preferred over resolving a least-
 342 square problem, which sometimes leads to unrealistic modal amplitudes into the high modes
 343 (Vic et al. 2023). The modal amplitudes x_n are calculated via a scalar product:

344
$$x_n = \int_{-980}^{-30} \psi_n(z) \cdot \zeta_{CTD}(z) dz \quad (6)$$

345 These amplitudes are then normalized by dividing with $\int_{-980}^{-30} \psi_n(z)^2 dz$. This analysis is
 346 restricted to the depth range from 30 m to 980 m in order to exclude the surface mixed layer
 347 while retaining the majority of available profiles along 23°W. The barotropic mode assumed to
 348 be zero. A vertical resolution of 10 m is used, with both the CTD profiles and World Ocean
 349 Atlas data interpolated accordingly. After computing the contribution of one mode, it is
 350 subtracted from the displacement profile: $\zeta'(z) = \zeta(z) - x_n \psi_n(z)$ and the procedure is
 351 repeated for the next mode. This recursive removal reduces cross-talk between modes caused
 352 by the limited vertical resolution and incomplete depth coverage. Since the order of mode
 353 extraction may influence the result, the decomposition is repeated $M = 100$ times with random
 354 permutations of modes $n = 1$ to $n = 20$, and the final modal amplitudes are calculated as the
 355 mean over all realizations, with associated standard errors.

356 **3.2. Potential vorticity and Rossby number**

357 Subsurface eddies exhibit signatures of high or low potential vorticity (PV), depending on their
 358 stratification anomaly and rotation direction (D'Asaro, 1988; McWilliams, 1985; Molemaker et
 359 al., 2015). In the absence of mixing, PV is a conserved quantity and serves as an effective
 360 tracer to differentiate water masses and track eddy pathways.

361 We refer to Ertels PV (Gill, 1982), being one of the most complete formulations for PV
 362 conservation, and take its vertical approximation (see e.g. Thomsen et al. (2016)), which is
 363 given by

$$Q = (\zeta_z + f) \cdot N^2 \quad (7)$$

364 where $\zeta_z = \frac{\partial v}{\partial x} - \frac{\partial u}{\partial y}$ is the vertical component of the relative vorticity with u and v being the zonal
 365 and meridional velocity, respectively, and f is the Coriolis parameter. The term $\zeta_z + f$
 366 represents the absolute vorticity. The approximation given by (7) is valid in case of nearly
 367 horizontally orientated isopycnal surfaces (Thomsen et al. 2016). Counter-clockwise and
 368 clockwise rotating eddies correspond to positive and negative relative vorticity, respectively. In

369 the northern hemisphere, anticyclonic eddies rotate clockwise and have negative relative
370 vorticity (vice versa for the southern hemisphere, which is not further considered throughout
371 this study).

372 In the case of geostrophic balance, the Rossby number

$$Ro = \frac{U}{Lf} = \left| \frac{\zeta_z}{f} \right| \quad (8)$$

373 where U is characteristic velocity and L is characteristic length scale, is smaller than one and
374 PV is always positive. PV can be reduced by either a reduction of N^2 (weakened stratification)
375 or by a gain of anticyclonic relative vorticity (D'Asaro, 1988). The explanation also applies vice
376 versa, i.e. PV can be increased by a strengthening in stratification or a gain of cyclonic relative
377 vorticity. The Rossby number becomes larger than one for submesoscale dynamics in the
378 ageostrophic range.

379 For the propagation speeds we followed an approach by Nof (1981) and Rubino et al. (2009),
380 who formulated the westward translation of isolated high baroclinic eddies on a plane, which
381 is given as a function of the n -th baroclinic Rossby radius of deformation and the Rossby
382 number:

$$C_n = -\frac{1}{3} \beta R_{d,n}^2 (1 - Ro)^{-1} \quad (9)$$

383 with β being the meridional derivative of the Coriolis parameter.

384 **3.3. Eddy identification algorithms**

385 **3.3.1. Eddy identification from shipboard observations**

386 Horizontal velocity data from the vmADCP system (see section 2.1) is used to detect eddies
387 along the 23°W meridian between 6°N and 12°N, following the methodology from Bendinger
388 et al. 2025. This methodology is based on an idealized eddy solution, known as Rankine vortex
389 characterized by solid-body rotation in its inner core, i.e., a linear increase of velocity with
390 increasing distance from the eddy center. We do so through the conversion from Cartesian
391 into cylindrical coordinates in areas that are suspected to cross eddies. Every point in the
392 horizontal plane is defined by the radial distance, r , to the origin (eddy center) and the
393 azimuthal angle, θ , i.e.:

394 $v_r = u \cos \theta + v \sin \theta$ (10)

395 $v_\theta = -u \sin \theta + v \cos \theta$ (11)

396 where v_r and v_θ are the radial and azimuthal velocities, respectively. Following Castelao and
 397 Johns (2011) and Castelao et al. (2013) the optimal eddy center is found by minimizing v_r
 398 (maximizing v_θ) via a non-linear least-squares Gauss-Newton algorithm.

399 $|v| = -u \sin(\theta) + v \cos(\theta) + \epsilon$ (12)

400 $\theta = \arctan(y_r / x_r)$ (13)

401 $y_r = y - y_c$ (14)

402 $x_r = x - x_c$, (15)

403 where (x, y) are the position vectors of the velocity samples, and (x_c, y_c) the eddy center
 404 location. The residual ϵ represents the radial velocity to be minimized. This methodology
 405 assumes a radially axisymmetric and non-translating vortex. Identifying the optimal eddy
 406 center allows us to analyze the circular (azimuthal) velocity around it. From this, we determine
 407 the eddy radius as the distance from the center where this velocity reaches its maximum -
 408 effectively separating the inner core of the eddy from its outer ring.

409 **3.3.2. Eddy identification in GFDL CM2.6 model**

410 From the GFDL CM2.6 model, we analyzed the position and trajectory of an individual
 411 simulated eddy that was representative in terms of its westward propagation in low latitude
 412 waters and its associated DO minimum. The horizontal eddy center was determined for each
 413 5-day model output and identified by locating the maximum of the streamfunction within a
 414 predefined $3^\circ \times 3^\circ$ longitude-latitude box centered on the eddy on a defined isopycnal surface.
 415 Once the position was found, we searched for the DO minimum around the eddy center within
 416 a $0.8^\circ \times 0.8^\circ$ horizontal box. On average, the deviation between the two positions was about
 417 20 km. Additionally, for each time step, we extracted the following variables: DO and salinity
 418 on isopycnal surface 26.5 kg m^{-3} , PV on the isopycnal surface 26.6 kg m^{-3} (corresponding to
 419 the isopycnal layer of minimum PV, see Fig. 4m), phosphate, and biomass integrated over the
 420 top 100 m, and particulate organic phosphorus at 100 m (to identify the downward flux of
 421 organic matter to the eddy core). To assess eddy anomalies, we compared these variables to
 422 their corresponding values outside the eddy (average over the area 1° to 3° longitude/latitude
 423 away from the eddy core), and also calculated the 20-year model mean at the eddy core
 424 position.

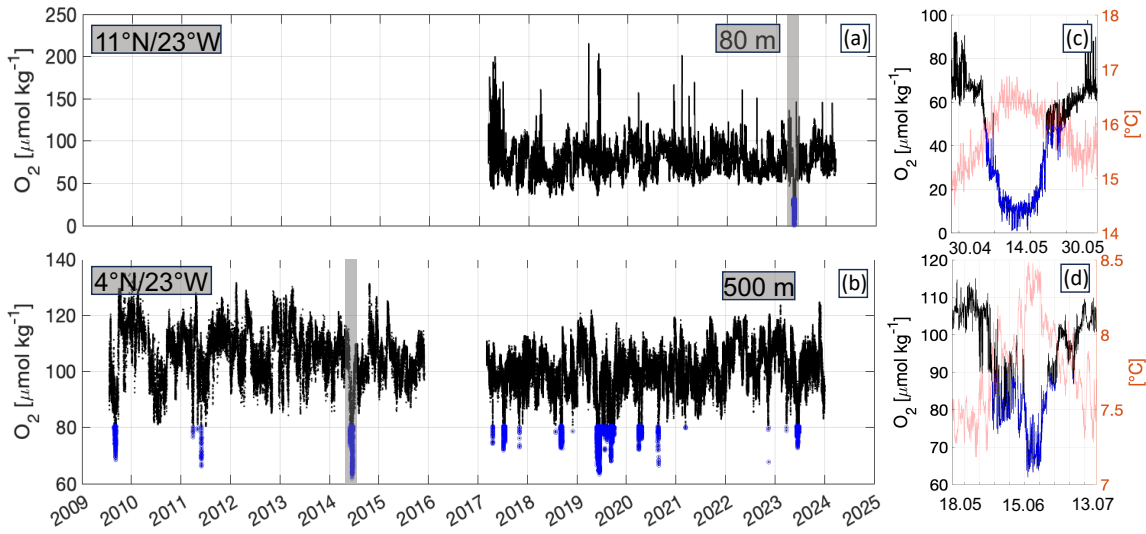
425 Around the eddy position, we identified the streamline with the strongest swirl velocity and
426 calculated the eddy radius $R = \frac{A}{2\pi i}$, assuming an isotropic circular eddy, where A is the
427 circumferences (length of contour). The swirl velocity U was calculated as the average of the
428 absolute value of the horizontal velocity along this contour. To estimate the propagation speed
429 (c), we tracked the eddy core positions at each time step, defined by the streamfunction
430 minimum. The speed was calculated as the horizontal distance between two successive eddy
431 centers divided by the time interval between them. To assess the isolative character of the
432 eddy, we calculated the isolation parameter U/c , where values greater than 1 indicate isolation
433 of the eddy core water from surrounding water masses.

434 **4. Results**

435 **4.1. Near-equatorial low-oxygen events: Frequency, magnitude and duration**

436 In all depth of the long-term DO time series from moored observations at 4°N and 11°N (both
437 at 23°W), recurring drops in DO levels are observed that fall significantly below the
438 climatological mean (Fig. 3 a, b or Fig. 1sup). A low-DO extreme event is defined based on the
439 interquartile range (IQR) of the respective time series, with events identified as values below
440 the lower quartile minus $1.5 \times \text{IQR}$. These events typically last from several days to a few
441 weeks and stand out clearly in the time series. They are often accompanied by a temperature
442 increase (Fig. 3c, d). On average, around two such events per year are observed at 4°N at
443 both 300 m and 500 m depth. At 11°N, about one event per year occurs at these depths, and
444 at 80 m only one strong event was detected within seven years. A similar pattern is found in
445 the moored time series from 11°N/21°W, where ten low-oxygen events ($40\text{--}60 \mu\text{mol kg}^{-1}$) were
446 recorded between 2012 and 2018 in the upper 200 m. Each event lasted about 3 - 4 weeks.

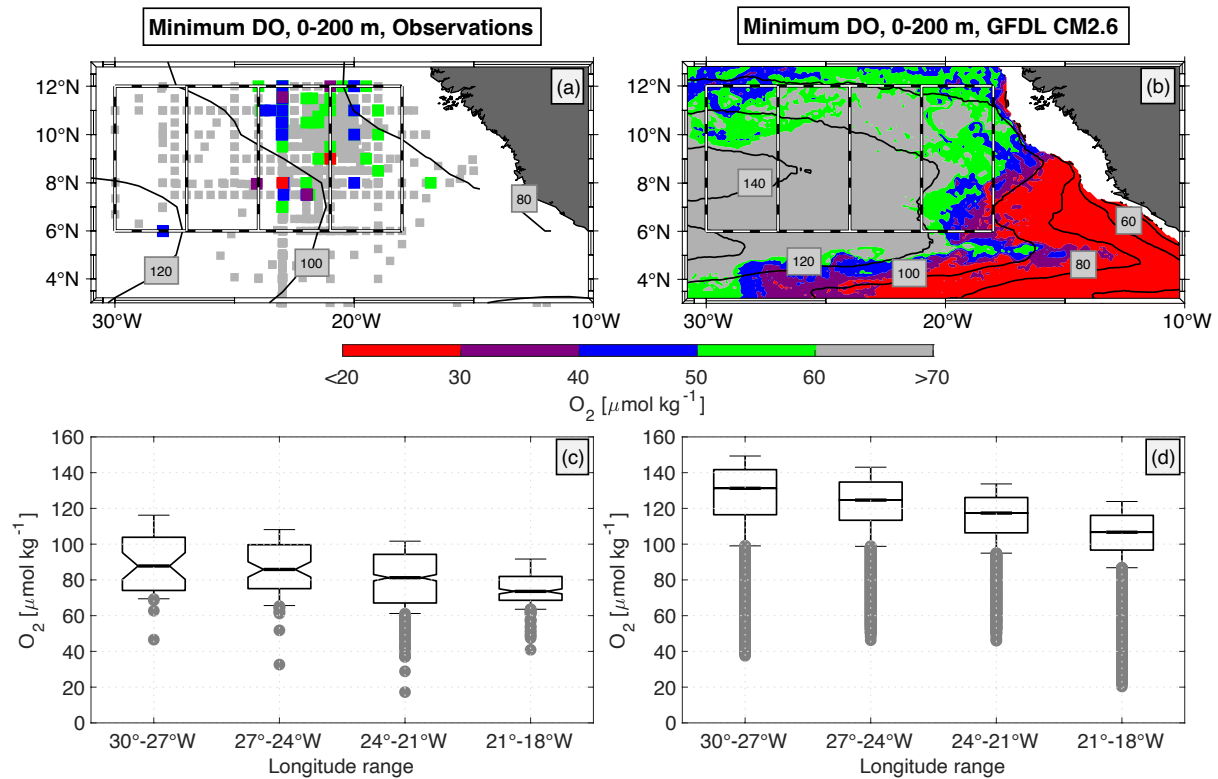
447 As expected, both the DO variability and amplitude of DO anomalies are generally greater at
448 shallower depths (e.g., 80 m), due to more intense near-surface dynamics and elevated
449 background DO concentrations. Therefore the largest DO drops were typically observed at 80
450 - 100 m. In terms of spatial variability, we see that the DO variability within the core of the deep
451 oxygen minimum zone (OMZ) at 11°N is generally lower than at 4°N.



452
453 Figure 3: Time series of observed DO at (a) 80m depth at 23°W, 11°N and 500 m depth at
454 23°W, 4°N shown in black. The blue color represent the lowest 10th percentile of the time
455 series data. The grey boxes mark the timespan (date on the x-axis) which is shown in (c) and
456 (d), where the temperature is overlaid in red.

457 In addition to the moored DO observations, there are multiple years of shipboard
458 measurements in the region. From all these shipboard observations, low-DO extremes are
459 identified by searching for the minimum DO concentration in the upper 200 m of every single
460 CTD-O profile. A low-DO extreme event was defined when DO was below a threshold of
461 60 $\mu\text{mol kg}^{-1}$, which represents the 10-percentile of all DO observations (74 of 976) in the area
462 6°-12°N, 30°-18°W (Fig. 4a and 4c). This threshold is more than 20 $\mu\text{mol kg}^{-1}$ below the
463 climatological DO concentration in the ETNA (Fig. 2a and 2b). Considering the absolute DO
464 concentration allowed us to derive a distribution of low-oxygen extremes, which is not masked
465 by the mean distribution. Lowest DO concentrations below 40 $\mu\text{mol kg}^{-1}$ (7 of 976 CTD-O
466 profiles) in the near equatorial region (south of 12°N) remarkably occurred not east of 21°W,
467 where profiles are located within a distance of 8° to the African coast, but in the “open-ocean”
468 region west of it (24°-21°W) (Fig. 4a). Further to the west (>24°W), lowest DO concentrations
469 were found again just above 40 $\mu\text{mol kg}^{-1}$. This is in contrast to the more coastal upwelling
470 region north of 12°N, where very low-DO extremes can also be observed near the coast (see
471 Fig. 1 or Schütte et al. 2016b). In order to scale for the different number of CTD-O profiles in
472 the four regions shown in Fig. 4a (5%, 9%, 61% and 25% of the profiles for the boxes 30°-
473 27°W, 27°-24°W, 24°-21°W, 21°-18°W), we estimated the relative distribution and calculated
474 the 10-percentile threshold in every box (Fig. 4c). This threshold is lowest in the open ocean
475 (24°-21°W), whereas the mean DO distribution is increasing from the eastern boundary
476 towards west. This counterintuitive distribution of low-oxygen extremes, which is against the

477 mean DO gradient, suggests that DO depleted water generally cannot be purely advected from
 478 a remote region at the eastern boundary, that is poor in DO. Locally enhanced biological
 479 activity associated with enhanced DO consumption must play a role as well.



480
 481 Figure 4: (a) Spatial distribution of DO profiles acquired from shipboard CTD-O observations
 482 in the tropical North Atlantic. Colored / gray dots denote DO profiles with a minimum DO
 483 concentration of lower / higher than $60 \mu\text{mol kg}^{-1}$ in the depth range 0-200 m (red: < 30
 484 $\mu\text{mol kg}^{-1}$, violet: $30-40 \mu\text{mol kg}^{-1}$, blue: $< 40-50 \mu\text{mol kg}^{-1}$, green: $< 50-60 \mu\text{mol kg}^{-1}$). (b)
 485 Horizontal distribution of DO minimum obtained in the depth range 0-200 m and from the last
 486 20 years of GFDL CM2.6 model run. Black contour lines in (a) and (b) show 0-200 m minimum
 487 of mean DO distribution (similar to filled contours in Fig. 2a and 2b). Dashed boxes denote
 488 different regions of interest for boxplots shown in (c) and (d). (c) Boxplots for 0-200 m minimum
 489 of DO profiles, that are shown for four different regions by the dashed boxes in (a). Thick line
 490 in each boxplot denotes median and notches show 95% confidence interval. Upper and lower
 491 whiskers denote 10% and 90% quantiles. Grey dots below the lower whiskers show 10%
 492 lowest DO events. (d) Similar to (c), but boxplots shown for 0-200 m minimum of DO profiles
 493 that were taken from the last 20 years of GFDL CM2.6 model run

494 The two events with the lowest dissolved oxygen (DO) concentrations were measured as 17
 495 $\mu\text{mol kg}^{-1}$ by a CTD at 60 m depth at $8^\circ\text{N}/23^\circ\text{W}$, while concentrations even below $5 \mu\text{mol kg}^{-1}$
 496 were recorded by a mooring at 80 m depth at $11^\circ\text{N}/23^\circ\text{W}$. These two low-oxygen extremes
 497 were well below the climatological average minimum DO concentration for the whole ETNA
 498 ($40 \mu\text{mol kg}^{-1}$ in the deep OMZ, Brandt et al. (2015)). We shall note, that no CTD-O profiles

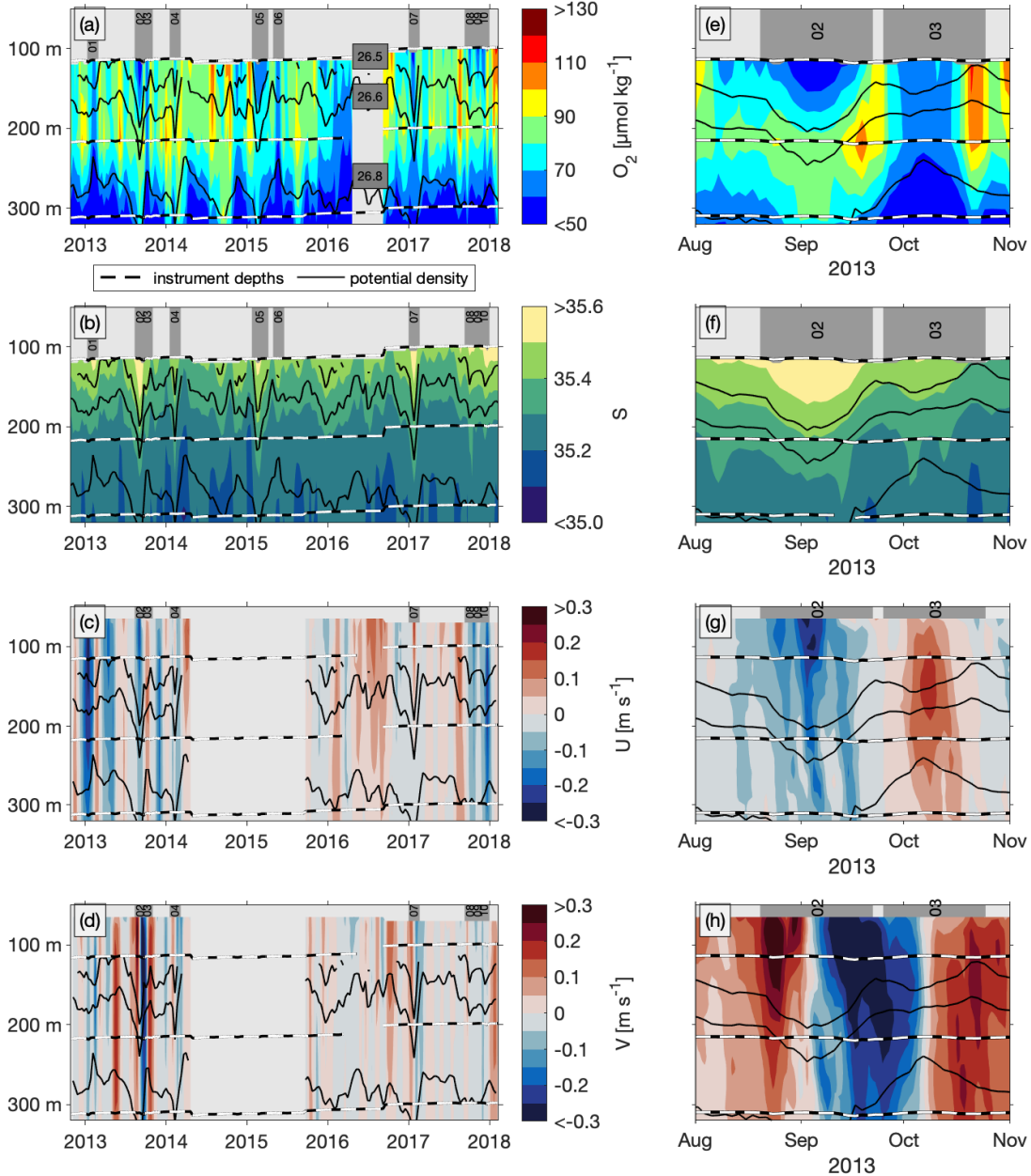
499 were available in this data set for the eastern boundary region within about 2° longitude off the
500 African coast.

501 **4.2 Association of low-oxygen events with subsurface high-baroclinic mode**
502 **vortices**

503 For the majority of the ship based data and for the mooring at 11°N/21°W additional
504 observations of hydrography, zonal and meridional velocity are available indicating the
505 passage of anticyclonically and cyclonically rotating vortices associated to the low-oxygen
506 events. At the mooring position the low-oxygen events #01, #02, #03, #04 and #07 were most
507 likely related to the passage of subsurface intensified vortices, whereof events #02, #04 and
508 #07 were associated with anticyclonic vortices and events #01 and #03 with cyclonic vortices
509 (Fig. 5). Note, that we explicitly refer here to the notation *vortex*, since we could not derive the
510 vortices' radii in order to differentiate between mesoscale and submesoscale. For the
511 anticyclonic vortices, meridional velocity was observed with maximum northward and
512 southward flow taking place at the beginning and the end of each low-DO period. Zero crossing
513 was observed in between at around the time, when DO was at its minimum (Fig. 5e to 5h).
514 Corresponding time series of potential density derived from hydrographic observations,
515 conducted next to the DO sensors, indicated a depression of isopycnal surfaces in the depth
516 range below 100 m. Time series of velocity and potential density agree well with the dynamical
517 understanding and passage of westward propagating eddies (van Leeuwen, 2007) through the
518 mooring site. Zonal velocity was either small or showed maximum flow during time periods of
519 minimum DO, depending whether the eddy has crossed the mooring site either with its core or
520 with one of its meridional flanks. Zonal velocity vanished at the beginning and the end of each
521 of the three events.

522 During events #01 and #03, that are associated with the passage of subsurface intensified
523 cyclonic vortices, we found a depression of isopycnal surfaces above 150 m and a heave of
524 isopycnal surfaces below ((cf. McGillicuddy (2015), denoted as eddies of type Thinny). This is
525 associated with a maximum in stratification at about 150 m depth. The time series of zonal and
526 meridional velocity, respectively, showed maximum values at a similar depth with a transition
527 from westward to eastward (event #01) and southward to northward (event #03) velocities
528 during the time of maximum stratification. In contrast to the anticyclonic vortex events (#02,
529 #04 and #07), the DO minima during the passage of the two cyclonic vortex events (#01 and
530 #03) were of similar intensity at 100 and 200 m depth, with no separation from the deep OMZ
531 at 300 m by an intermediate DO maximum. Though, during both events the minimum DO at
532 100 m was well below the average DO concentration that was observed for time periods

533 without any vortex event. We shall explicitly note, that the characteristics for zonal and
 534 meridional velocity during event #01 were swapped compared to the other eddy events (#02,
 535 #03, #04 and #07). We can only speculate whether this cyclonic vortex has crossed the
 536 mooring site in a more meridionally directed pathway.



537
 538 Figure 5: Time series of observed (a) DO, (b) salinity, (c) eastward and (d) northward velocity
 539 from moored observations at 11°N/21°W in the upper 300 m as a 10-day average (color
 540 shading). Black lines denote depth of potential density surfaces 26.5, 26.6 and 26.8 kg m^{-3} .
 541 Black-white dashed lines denote depths of DO sensors (in (a), (c) and (d)) and salinity sensors
 542 (in (b)). Gray bars with numbers 01-10 in the top of these panels denote time periods of low-
 543 DO events (#01 to #10). Note, that no velocity observations are available for low-DO events
 544 #05 and #06. Panels (e)-(h) show corresponding 2-day averaged time series for the 90-day
 545 time period around low-DO events #02 and #03.

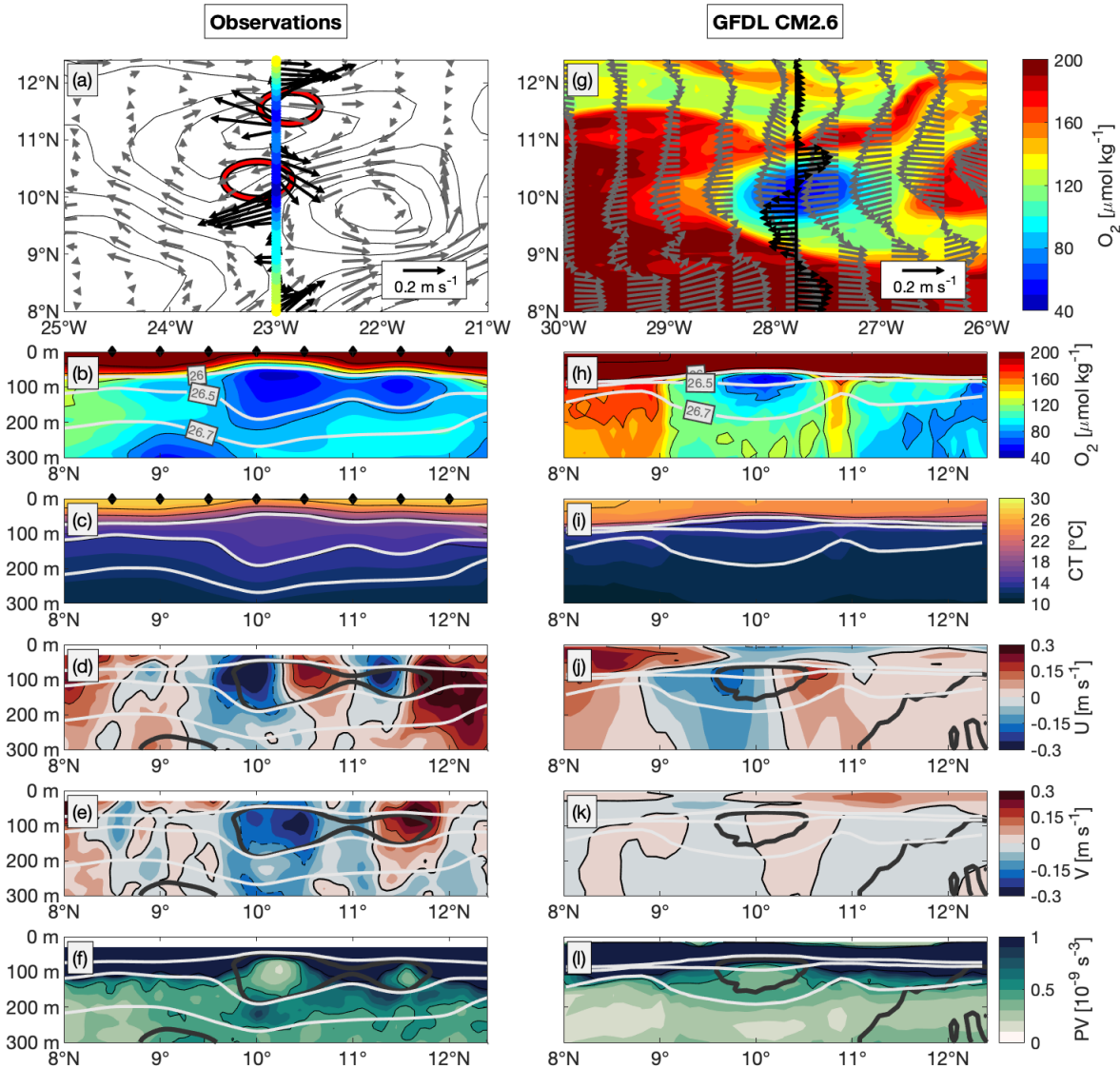
546 The vertical structure of these vortices could not be identified for the near surface layer and
547 the deep ocean, since moored hydrographic and velocity observations were only available
548 between 100 m (60 m for velocity) and 800 m depth. This made it challenging to distinguish
549 among surface intensified and subsurface intensified (but at shallow depth) vortices. The most
550 likely subsurface intensified vortex was associated with event #02, showing extreme velocity
551 (both zonal and meridional) slightly below the shallowest depth of available observation
552 accompanied by an oxygen minimum of $39 \mu\text{mol kg}^{-1}$. Notably, none of these vortices exhibited
553 a clear surface signature in satellite data that could be unambiguously associated with the
554 subsurface features

555 **4.3 Horizontal extent of the low-oxygen high-baroclinic mode vortices**

556 The ship-based data, which cover the region spatially, are significantly better suited than the
557 stationary moored data for assessing the spatial extent of the HBVs. Repeated meridional ship
558 sections between $6\text{--}12^\circ\text{N}$ along 23°W , available over a distance of at least 300 km, captured
559 15 events with DO concentrations well below $60 \mu\text{mol kg}^{-1}$ in the upper 200 m (Table 1, Fig.
560 6,). All DO minima were found directly below the shallow oxycline at depths between 45 and
561 90 m (corresponding to surfaces of potential density between $\sigma_\theta = 26.2$ and 26.4 kg m^{-3}). The
562 meridional resolution of CTD-O measurements did not allow for a proper identification of the
563 meridional core position of the low-DO extremes, but their extent was found with roughly 1° in
564 latitude in maximum. The low-DO cores vertically extended to the isopycnal $\sigma_\theta = 26.5 \text{ kg m}^{-3}$
565 (150 m depth) and were separated from the deep OMZ by an intermediate DO maximum
566 located at about $\sigma_\theta = 26.7 \text{ kg m}^{-3}$ (between 200 and 300 m), which rules out a simple vertical
567 displacement of the vertical gradient.

568 We analyzed the distribution of zonal and meridional velocity at the depth of the DO minimum
569 using an eddy identification algorithm as described in *section 3.3.1*. Strikingly, 66% (10 of 15)
570 of the low-DO events could be related to HBVs, where radii were identified between 20 and 45
571 km (average 34 km) (Table 1 Fig. 6b and 6d). The radii are substantially smaller than the typical
572 mesoscale (first baroclinic Rossby radius of deformation) at these latitudes being at the order
573 of 100 km or more. Instead, these eddies have a confined baroclinic structure, which is
574 associated to higher baroclinic modes and corresponding smaller Rossby radii of deformation
575 as is shown in detail in *section 4.4*. The HBVs' horizontal core positions are estimated from the
576 current velocities and closely match the meridional position of the low-oxygen extremes (cf. 3rd
577 and 6th column for bold marked events in Table 1; Fig. 6a and 6b). Note, that the derived HBVs'
578 zonal core position range between 23.3°W and 22.9°W , whereas for the low-oxygen extremes,
579 only the meridional position along the 23°W section can be identified. Notable is the

580 simultaneous occurrence of two HBVs observed during one cruise in 2009 at positions
 581 10.3°N/23.2°W and 11.6°N/22.9°W (Fig. 6a to 6f). These two HBVs were meridionally cut
 582 through their eastern and western flank, respectively, and were both observed with DO
 583 concentrations well below 50 $\mu\text{mol kg}^{-1}$ (Fig. 6a and 6b).



584
 585 Figure 6: (a) Current velocity (black arrows) and DO (colored dots) at 80 m depth along 23°W
 586 and between 8° and 12°N obtained from along-track shipboard ADCP observations and
 587 CTD-O observations between 23-Jul-2009 and 25-Jul-2009 (cruise Ron Brown 2009, see
 588 Table 1). Grey arrows show geostrophic velocities and black contours show sea level
 589 anomalies from satellite altimetry data on 24-Jul-2009. Red circles denote positions and extent
 590 of the two eddies, identified and reconstructed from shipboard ADCP observations at 80 m.
 591 Latitude-depth sections of (b) DO, (c) conservative temperature, (d) zonal velocity, (e)
 592 meridional velocity and (f) PV between 8° and 12°N obtained from CTD-O observations along
 593 23°W (same period to (a)). Black diamonds at the top of panels (b) and (c) denote actual
 594 latitudes of CTD-O profiles. Thin gray lines in panels (b) to (f) denote surfaces of potential
 595 density. In panels (d)-(e), solid black and dashed black lines denote 0.15 m s^{-1} velocity
 596 intervals. Thick dark gray lines in panels (d)-(f) denote DO contours of 70 $\mu\text{mol kg}^{-1}$. (g)-(l) are
 597 analog to (a)-(f), but taken from GFDL CM2.6 model simulation for model date 23-Mar-0197.
 598 Gray arrows in (g) denote surface velocity. Black arrows denote current velocity and colored

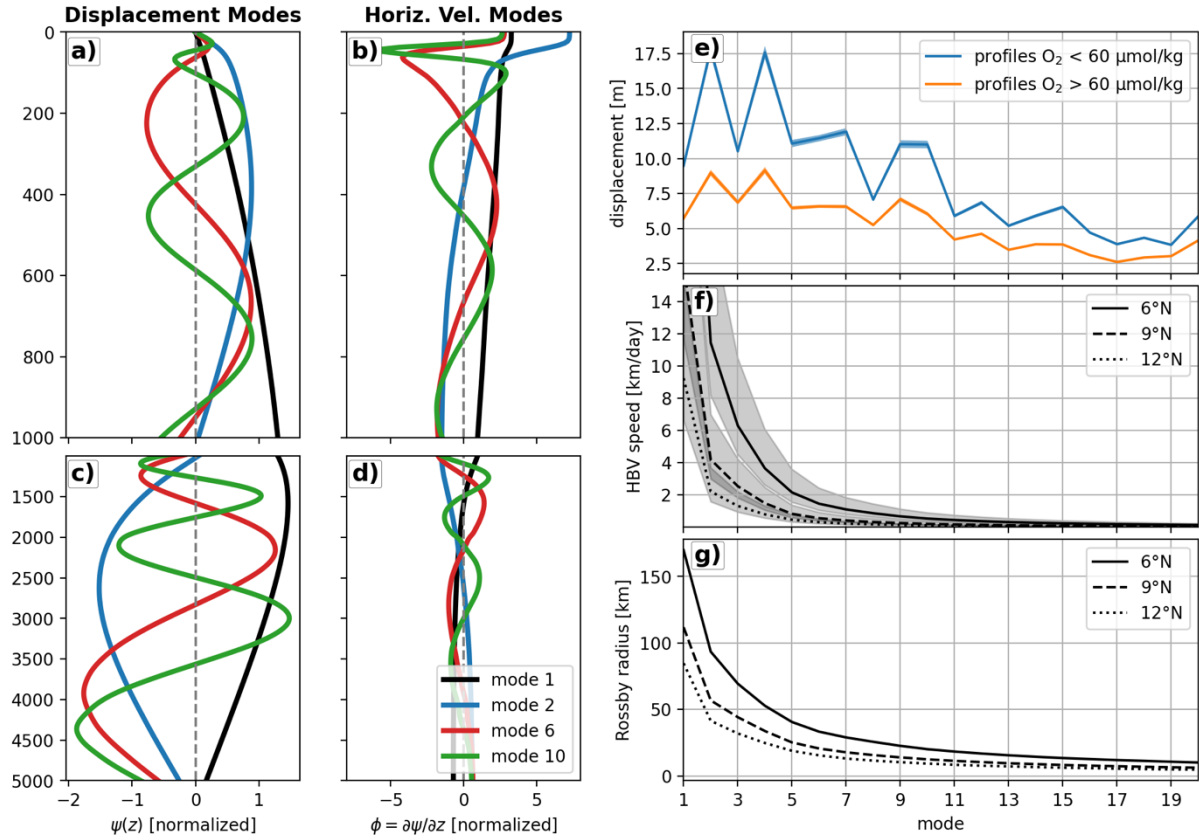
599 contours show DO distribution both at 77 m depth along $\sim 28^{\circ}\text{W}$. (h) to (l) show respective
600 latitude-depth sections along $\sim 28^{\circ}\text{W}$ for the same model date. Thick dark gray lines in panels
601 (j)-(l) denote DO contours of $90 \mu\text{mol kg}^{-1}$.

602 Both HBVs were identified to be anticyclonic and subsurface intensified, as shown by the
603 anomalously weak stratification along 23°W at subsurface depth, which is indicated by the
604 thickening of isothermal and isopycnal layers at the depth range of the DO minimum core (Fig.
605 6c). The vertical extent of the HBVs (characterized by displaced isopycnal surfaces or zonal
606 velocity) reached at least down to about 250 m and covered the vertical extent of the low-DO
607 cores. The estimated radii are 36 and 31 km and thus considerably smaller than the first
608 baroclinic Rossby radius of around 90 km at these latitudes. For none of the 10 anticyclonic
609 HBVs, we could identify any anticyclonic signature from satellite altimetry observations (Fig.
610 6a). One reason might be that the resolution of gridded SLA from conventional altimetry
611 (in time and space) is not sufficient to resolve such small-scale features. Another reason could
612 be the fact that the eddies are strongly confined to the thermocline (below 30 – 50 m) and often
613 do not have a surface signature.

614 **4.4 Vertical structure of low-oxygen high-baroclinic mode vortices**

615 The decomposition of a disturbed density profile into vertical baroclinic modes gives evidence
616 about both the theoretical radius (Rossby radius) and propagation speed for this disturbed
617 state (see *section 3.1*). Here, we did a vertical baroclinic mode analysis for the meridional
618 section along 23°W between 6 and 12°N , which allowed us a direct comparison against the
619 spatially resolved low-DO HBVs observed during the respective ship sections. The vertical
620 structure of the first 20 baroclinic modes was obtained from the climatological hydrographic
621 distribution (Fig. 7a to 7d). For all individual CTD-O profiles, we derived displacement profiles,
622 ξ , and calculated vertical mode amplitudes x_n via modal decomposition (as described in
623 *section 3.1*). We then clustered all x_n (i) related to a low-DO event (Table 1) and (ii) not related
624 to a low-DO event (i.e. all other profiles along 23°W between 6 and 12°N), and calculated an
625 average amplitude distribution (Figure 7e). For low-DO events, we found substantially
626 enhanced amplitudes at all modes, but particularly at mode 2, 4, 7, 9 and 10 compared to the
627 average amplitude distribution that is related to no low-DO events (Fig. 7e). These higher
628 baroclinic modes $n > 4$ (exemplarily shown for mode 6 and 10 for $9^{\circ}\text{N}/23^{\circ}\text{W}$ in Fig. 7a and 7c
629 for vertical displacement and pressure/horizontal velocity, respectively) have zero crossings in
630 the upper few hundred meters, that are of similar vertical length scale compared to the vertical
631 extent of low-DO HBVs (near-surface to 250 m, see *section 4.2.1*). The lower baroclinic modes
632 (e.g. mode 2) have a much larger vertical length scale and are not capable of describing the
633 vertical structure that is related to low-DO HBVs. The corresponding Rossby radius of

634 deformation for vertical baroclinic modes 4 to 10 was found from $R_{d,4} = 47$ km to $R_{d,10} = 18$ km
 635 at $6^\circ\text{N}/23^\circ\text{W}$ and from $R_{d,4} = 24$ km to $R_{d,10} = 9$ km at $12^\circ\text{N}/23^\circ\text{W}$ (Fig. 7g). These radii are well
 636 below the first baroclinic Rossby radius of deformation ($R_{d,1} = 152$ km at $6^\circ\text{N}/23^\circ\text{W}$ and $R_{d,1} =$
 637 80 km at $12^\circ\text{N}/23^\circ\text{W}$) and are close to the average radius of 34 km that was identified for the
 638 observed low-DO eddies (cf. Table 1 and section 4.3).

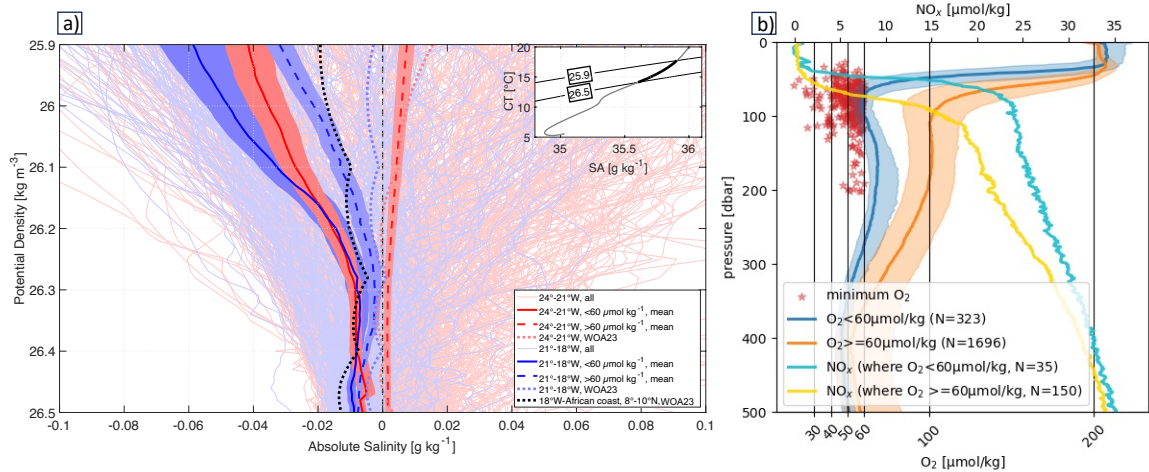


639

640 Figure 7: Dimensionless vertical structure functions of baroclinic modes 1, 2, 6 and 10 for (a,
 641 b) isopycnal displacement, Ψ_n , and (c, d) horizontal velocity, ϕ_n , obtained from the
 642 hydrographic profile of the World Ocean Atlas at $9^\circ\text{N}/23^\circ\text{W}$. (a) and (c) ((b) and (d)) show depth
 643 range 0 to 1000 m (1000 m to bottom). (e) Mean amplitudes of first 20 vertical displacement
 644 modes calculated through modal projection of hydrographic profiles from 23°W ship sections.
 645 Blue solid line denotes mean amplitude distribution, that is related to all hydrographic profiles
 646 with a minimum DO smaller than $60 \mu\text{mol kg}^{-1}$ in the upper 200 m (i.e. low-DO events that are
 647 summarized in Table 1). Orange solid line denotes mean amplitude distribution for all other
 648 hydrographic profiles along 23°W . Respective shadings denote standard error of the mean
 649 amplitude over all 1000 realizations. (f) Theoretical translation speed of high-baroclinic Rossby
 650 waves (HBVs) for the first 20 vertical modes between 6°N and 12°N along 23°W (see equation
 651 9). The solid, dashed and dotted black lines represent $\text{Ro} = 0.5$, while the shaded area
 652 indicates the range $0.3 < \text{Ro} < 0.7$.
 653 (g) Rossby radii of deformation for the first 20 vertical modes. In both (f) and (g), solid, dashed,
 654 and dotted lines correspond to values at 6°N , 9°N , and 12°N along 23°W , respectively.

655 **4.5 Source waters of high-baroclinic mode vorticies**

656 The determination of the physical origin of subsurface HBVs, that are associated with the
 657 observed low-DO events, is not straight forward. A backtracking algorithm based on satellite
 658 altimetry observations as used in other studies for more poleward eddies (Chelton et al., 2011;
 659 Schütte et al., 2016a) is not applicable here, since these near-equatorial HBVs are hardly
 660 captured in the respective SLA products (Fig. 6). Instead, we derived water mass
 661 characteristics from all CTD-O profiles (Fig. 4a) located in the two boxes [24°-21°W, 6°-12°N]
 662 and [21°-18°W, 6°-12°N] for a conservative temperature range that corresponded to the depth
 663 range of the shallow DO minimum. A mean profile of absolute salinity was calculated for the
 664 two boxes and was used as a reference in order to calculate anomalies of absolute salinity as
 665 a function of potential density for every single CTD-O profile (Fig. 8). For both boxes, we
 666 clustered the salinity anomaly profiles into two classes, that were defined by the minimum DO
 667 concentration in the upper 200 m to be either below or above the threshold of 60 $\mu\text{mol kg}^{-1}$.



668

669 Figure 8: a) (Large panel) Anomalies of absolute salinity as a function of potential density in
 670 the eastern tropical North Atlantic for two different box regimes (Red: 24°-21°W, 6°-12°N /
 671 Blue: 21°-18°W, 6°-12°N). The boxes are highlighted in Fig. 4. The anomalies are referenced
 672 to the mean profile of absolute salinity that was calculated from all hydrographic profiles found
 673 in both boxes. Thin solid lines denote all individual profiles and thick solid (dashed) lines show
 674 the average of the profiles, that are related to minimum DO concentrations below (above)
 675 60 $\mu\text{mol kg}^{-1}$ in the upper 200m. Shadings to the average profiles illustrate the respective
 676 standard errors (see text for details). Blue and red dotted lines denote climatological profiles
 677 for the two boxes. Black dotted line shows the climatological profile for a third box (18°W-
 678 African coast, 8°-10°N), which defines the near-coastal regime off West-Africa. (Inset panel)
 679 Mean characteristics of absolute salinity versus conservative temperature for the box 24°-
 680 18°W, 6°-12°N, taken from all CTD-O observations in this regime. Thick black line denotes the
 681 characteristics in the potential density range 25.9 to 26.5 kg m^{-3} and is the reference profile for
 682 the anomalies shown in the large panel. b) The blue curve shows the median of all oxygen
 683 CTD profiles with a minimum below 60 $\mu\text{mol/kg}$ in the upper 200 m. The red stars indicate the
 684 depths and dissolved oxygen concentration of these minima. Orange curves represent profiles
 685 with a minimum above 60 $\mu\text{mol/kg}$. Shaded areas indicate the standard deviation. The
 686 turquoise line depicts the mean nitrate profile for the profiles with oxygen minima below 60

687 $\mu\text{mol/kg}$, and the yellow line shows the mean nitrate profile for the profiles with minima above
688 $60 \mu\text{mol/kg}$.

689 Along-isopycnal gradients of mean salinity are weak (i.e. small spiciness) in the considered
690 region [24°W-African coast, 6°-12°N], as shown by the water mass characteristics obtained
691 from the climatological distribution (World Ocean Atlas 2023) for the two boxes as well as for
692 the near-coastal area east of them. The westward salinity increase along isopycnal surfaces
693 is roughly 0.01 to 0.02 g kg^{-1} per 5° (from the African coast at 17°W to about 22°W) in the
694 potential density range between 26.1 and 26.4 kg m^{-3} . This weak isopycnal gradient does not
695 allow for a differentiation of water mass characteristics from individual CTD-O profiles.

696 However, water mass characteristics for low-DO and high-DO profiles were found to be
697 significantly different from each other, when isopycnally averaging over all respective profiles.
698 For the western box [24°-21°W, 6°-12°N], low-DO profiles were on average lower in salinity
699 (compared to high-DO profiles) and they were found to be close to the average salinity anomaly
700 profile from the eastern box [21°-18°W, 6°-12°N], suggesting that water masses related to low-
701 DO profiles have their origin closer to the eastern boundary. However, the tropical low-DO
702 extremes appear in the open ocean far away from the eastern boundary. The westward
703 intensification of these events (section 4.1, Fig. 4), that are often related to HBVs (section 4.2),
704 suggests an unexpected long isolation of the DO depleted water masses in the otherwise
705 oxygen rich open ocean.

706 To further support the persistence and longevity of HBVs, we analyzed CTD observations of
707 oxygen and nitrate inside and outside of low-oxygen events. Fig. 8b shows the median oxygen
708 profiles for CTD casts with a minimum in the upper 200 m of the water column below 60
709 $\mu\text{mol/kg}$ (blue curve) and those above $60 \mu\text{mol/kg}$ (orange curves). Mixed layer oxygen
710 concentrations for both cases indicate increased near-surface biological productivity of HBVs
711 compared to outside of HBVs. The red stars indicate the depths and dissolved oxygen
712 concentrations of the observed oxygen minima, clustering between 80 to 120m depth.
713 Corresponding nitrate profiles are shown in turquoise ($<60 \mu\text{mol/kg}$ oxygen) and yellow (>60
714 $\mu\text{mol/kg}$ oxygen). The results reveal substantially lower oxygen concentrations between 80 -
715 250 m inside HBVs, accompanied by elevated nitrate levels, consistent with enhanced
716 accumulated ongoing biologically remineralization due to enhanced productivity and/or “older”
717 water. This observational evidence indicates that HBVs consist of persistent, isolated water
718 masses rather than short-lived anomalies.

719 **4.6 Origin & temporal evolution of high-baroclinic mode vorticies based on model**
720 **simulations**

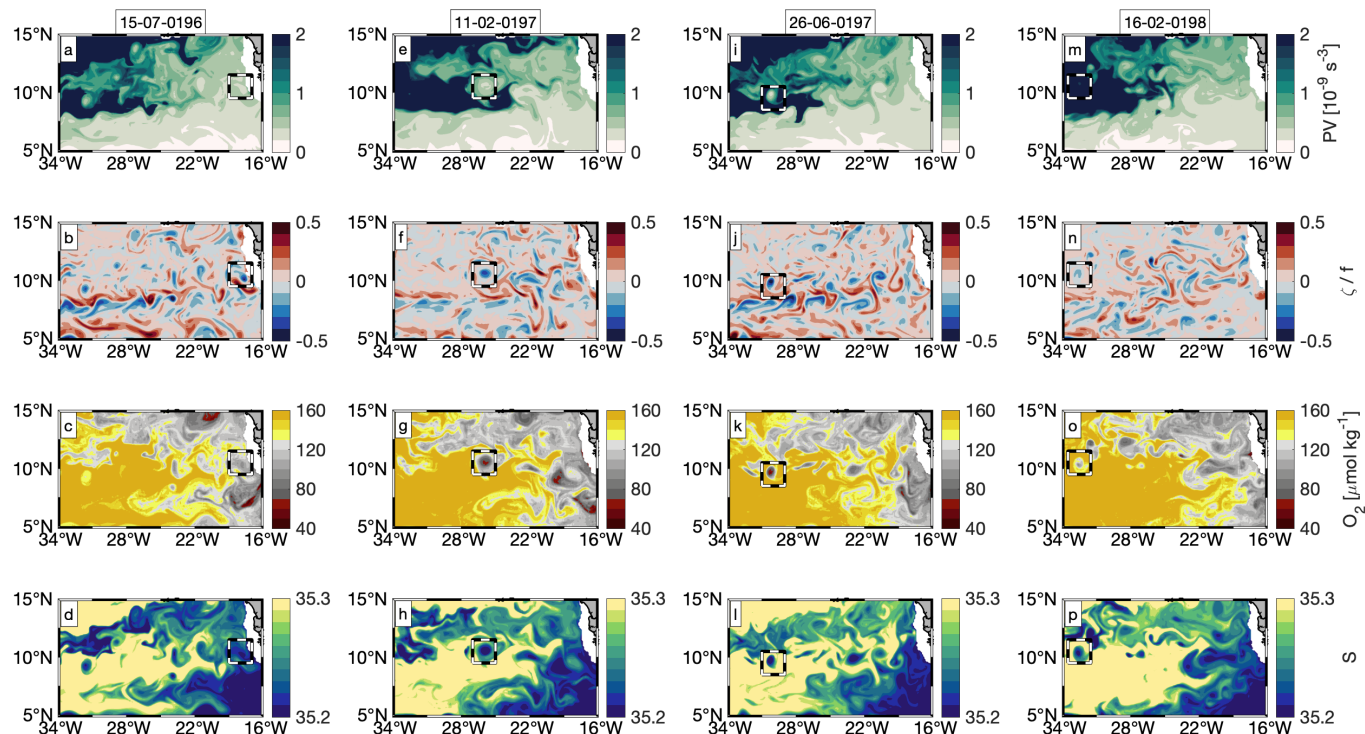
721 Outputs from the GFDL CM2.6 ocean model is used to investigate the origin and temporal
722 evolution of these unusual vortices. We used the last 20 years of simulations for a regime
723 similar to that considered in the shipboard observations. From Fig. 2, we already know that the
724 model captures the main features of the mean state of the oxygen distribution. To assess
725 whether low-oxygen events occur with similar frequency in the model and whether they are
726 likewise associated with HBVs, we conducted analyses analogous to those performed on the
727 observations (*Section 4.1*, Fig. 4; and *Section 4.3*, Fig. 6) using the model data.

728 First the horizontal DO distribution was calculated by taking the temporal and vertical (0-200 m)
729 minimum of the simulated DO similar to the observations (Fig. 4b). In the latitude range 6°-
730 12°N, lowest DO below 30 $\mu\text{mol kg}^{-1}$ is found close to the African coast (east of 18°W). In
731 general, the basin wide gradient of minimum DO is positive towards west, being in agreement
732 with the zonal gradient of the mean simulated DO distribution (Fig. 2b). Strikingly, minimum
733 DO is lower in the region 30°-24°W, 8°-12°N than in the region east of it (24°-21°W). The
734 threshold for the DO 10-percentile (100 $\mu\text{mol kg}^{-1}$) does not change over this longitude range,
735 whereas the mean DO distribution is increasing towards west (lower whiskers versus box
736 centers in Fig. 4d). The open ocean minimum of the DO distribution that is found in the region
737 30°-24°W, 8°-12°N is in good qualitative agreement (though located further west) with the
738 observed DO distribution (Fig. 4b versus Fig. 4a). In the longitude range 24°-21°W, low-oxygen
739 events are less likely. It should be noted that Fig. 4a and 4b compare individual shipboard
740 observations with the 20-year model climatology. Observations represent snapshots of specific
741 events, whereas the model averages over a longer temporal period. Consequently, apparent
742 differences in the zonal distribution of low-DO extremes are expected and do not necessarily
743 indicate a systematic model bias.

744 From the GFDL CM2.6 model, we identified a HBV with a low-DO core in the near-equatorial
745 open ocean as exemplarily shown at the position 10°N/28°W (Fig. 6g to 6l). The spatial extent
746 is comparable to our observational results (Fig. 6a to 6f). A meridional cross section through
747 the simulated HBV reveals the low-DO core at 80 m depth (isopycnal surface 26.5 kg m^{-3}) with
748 a lateral extent of about 1° in latitude and a vertical extent between about 50 and 150 m (Fig.
749 6h). The minimum DO is lower than 60 $\mu\text{mol kg}^{-1}$, whereas DO outside the HBV is at values
750 above 150 $\mu\text{mol kg}^{-1}$. Distributions of conservative temperature and potential density show
751 shallowing and deepening isopycnal surfaces above and below the DO minimum, respectively,
752 indicating a weakened stratification and consequently low PV at the low-DO core (Fig. 6i). The
753 HBV's velocity signature is strongly confined to subsurface depths and vanishes above 50 m
754 (Fig. 6j,6k). In particular, surface velocity does not show any coherence with the subsurface
755 velocity field at depth of the HBV (Fig. 6g). This substantiates our observational results that
756 these HBVs can hardly be identified from the surface geostrophic velocity field obtained from

757 satellite observations. The HBV core exhibits low PV water, where minimum PV is found
 758 slightly deeper than the DO minimum (Fig. 6l). This low PV water core is laterally isolated from
 759 the surrounding high PV water, but also separated from the deeper low PV water through an
 760 intermediate PV maximum along the isopycnal surface 26.7 kg m^{-3} . This isolation is the
 761 prerequisite for a persistent eddy with a long-life time. The model tends to slightly
 762 underestimate PV and associated O_2 anomalies, indicating somewhat weaker eddy coherence
 763 compared to observations. At the same time, due to reduced dissipation in the circulation
 764 model, we expect lifespans of the eddies to be slightly prolonged. Additionally, the MiniBLING
 765 model does not fully account for remineralization processes in the mesopelagic zone, which
 766 likely leads to an underestimation of oxygen consumption. Taken together, this implies that
 767 HBVs in the model appear with weaker anomalies but with an artificially prolonged lifespan.

768 In the following, we present the temporal evolution of the HBV from the time of formation to the
 769 decay. Fig. 9 shows model snapshots with horizontal maps of PV, relative vorticity normalized
 770 by f (so that its magnitude is equal to Rossby number), DO and salinity for four different time
 771 points throughout the HBV's lifetime. Fig. 10 shows time series of different physical and
 772 biogeochemical variables for the HBV core position.

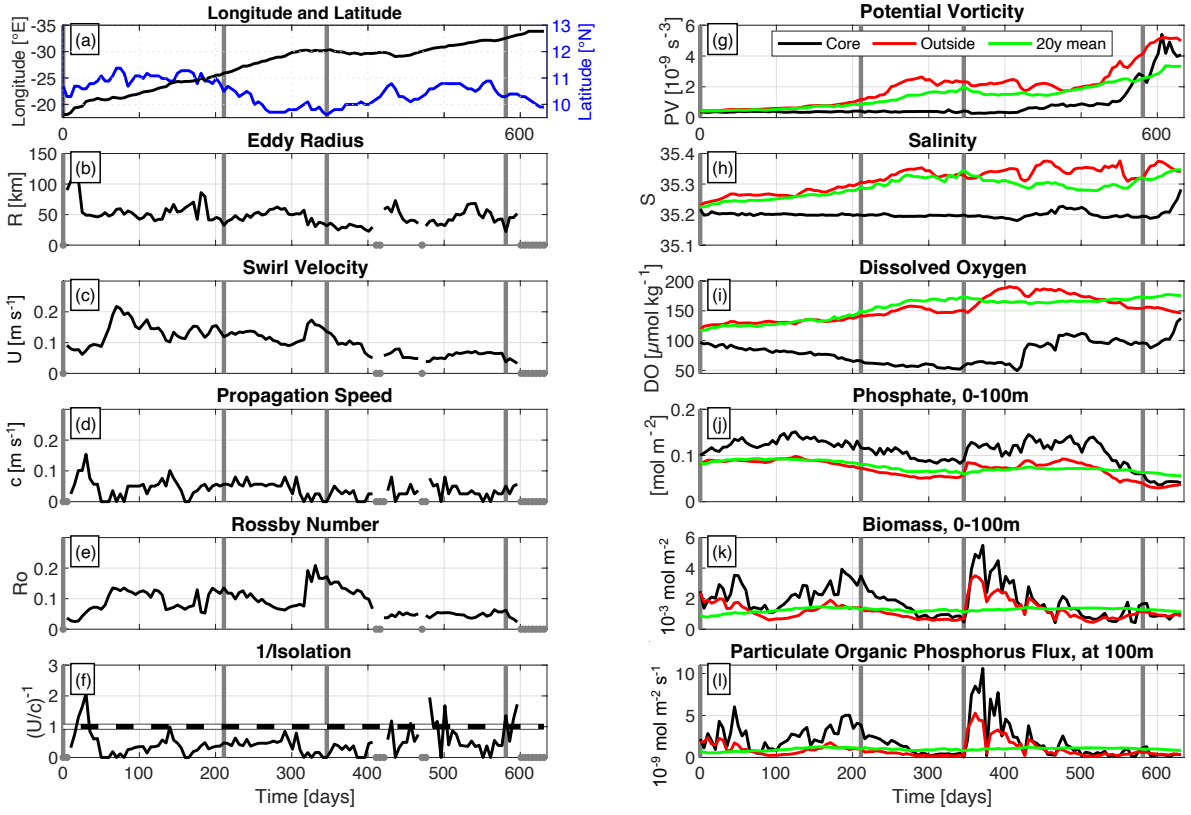


773
 774 Figure 9: Model snapshots of PV on isopycnal surface 26.6 kg m^{-3} (top row), relative vorticity
 775 over f , DO and salinity on isopycnal surface 26.5 kg m^{-3} (second, third and fourth row) for
 776 different phases (different columns) of an anticyclonic HBV (respective time indicated above

777 each column with $T = 0 / 211 / 346 / 580$ days: formation / strongest peculiarity / weakening /
778 decay. Black-white dashed box in each sub panel denotes HBV position.

779 The HBV has its origin at the eastern boundary at $10^{\circ}\text{N}/18^{\circ}\text{W}$, where low PV water (Fig. 9a)
780 with anticyclonic vorticity (Fig. 9b) is deflected offshore and provides the precondition for the
781 eddy formation. The offshore deflected water carries typical water mass characteristics from
782 the eastern boundary: low DO and low salinity (Fig. 9c and 9d). During westward propagation
783 into the open ocean, the HBV enters high PV waters. 211 days after formation, it reaches
784 $10.5^{\circ}\text{N}/26^{\circ}\text{W}$ with low PV (Fig. 9e) and high negative relative vorticity (Fig. 9f) in its core. The
785 coherent eddy is strongly isolated from surrounding high PV water as shown by the intensified
786 DO minimum (Fig. 9g) and low salinity (Fig. 9h) in its core. In the following 5 months the HBV
787 propagates further westward, but is disturbed by high PV water, that is advected from the
788 western tropical Atlantic. This leads to a weakening of the HBV with a smaller low PV core
789 (Fig. 9i), but still carrying pronounced negative relative vorticity (Fig. 9j), low DO (Fig. 9k) and
790 low salinity (Fig. 9l) compared to surrounding water. The HBV eventually loses its energy and
791 decays about 580 days after formation at $10^{\circ}\text{N}/33^{\circ}\text{W}$ (Fig. 9m and 9n), where the core water
792 still appears with anomalous low DO and salinity (Fig. 9o and 9p).

793 The quick offshore deflection of coastal water, that is associated with the HBV's formation, is
794 illustrated by the strong change in longitude (Fig. 10a) and by the high propagation speed (Fig.
795 10d) during the first 50 days. This deflection is more like a pulse rather than an offshore
796 transport of enclosed water ($(U/c)^{-1} > 1$, Fig. 10f), where the HBV stabilizes after that time at
797 a radius of 50 km (Fig. 10b).



798

799 Figure 10: Time series of different variables related to the core of the modelled subsurface
800 intensified eddy shown in Figs. 4h-4n and Fig. 8. Time is given as elapsed days since eddy
801 detachment from the African coast. Vertical gray lines in each panel denote time points for
802 horizontal maps shown in Fig. 9 (0, 211, 346 and 581 days). (a) longitude (black line) and
803 latitude (blue line), (b) Eddy radius, (c) Eddy swirl velocity, (d) Eddy propagation speed, (e)
804 Rossby number, (f) Inverse of isolation parameter (black line). Black-white dashed line denotes
805 threshold, below which the water is trapped in the eddy core (swirl velocity > propagation
806 speed). (g) Potential vorticity, (h) salinity, (i) DO, (j) phosphate, (k) biomass, (l) flux of
807 particulate organic phosphorus. Variables are given for the following layers. In panels (a)-(f)
808 and (h)-(i): isopycnal surface 26.5 kg m^{-3} . In panel (g): isopycnal surface 26.6 kg m^{-3} . In panels
809 (j)-(k): integral over 0-100 m. (l) at 100 m. For the right column (panels (g)-(l)), black lines show
810 value in eddy core, red lines show mean values outside the eddy (average between 1° and 3°
811 of longitude/latitude around the eddy core position) and green lines show 20-year model mean
812 that is given at the respective position of the eddy core. In panels (b)-(f), gray dots at zero line
813 denote time points, where no estimate was possible.

814 From day 80 to day 300, the HBV continuously propagates westward until 30°W with only slight
815 changes in latitude (10° - 11°N), at a propagation speed of 0.7 m s^{-1} , a swirl velocity between
816 0.1 and 0.2 m s^{-1} and a radius of 50 km (Rossby number between 0.1 and 0.2) (Fig. 10a-10f).
817 The strong isolation ($(U/c)^{-1} < 1$) over that time keeps the core water constantly low in PV
818 and salinity, while surrounding waters increase in PV and salinity during eddy westward
819 propagation (Fig. 10g-10h). DO continuously decreases from roughly $95 \mu\text{mol kg}^{-1}$ to
820 $50 \mu\text{mol kg}^{-1}$ over several months, corresponding to an average DO consumption rate of about
821 $0.16 \mu\text{mol kg}^{-1} \text{ d}^{-1}$ (Fig. 10i). This apparent decline should be regarded as a lower limit, as
822 ventilation and mixing processes would partly offset oxygen loss. In the upper part of the eddy,

823 enhanced nutrient concentration is associated with increased biomass production, which leads
824 to enhanced export of organic matter between days 100 and 300 (Fig. 10j-10l). The associated
825 increased respiration and the strong isolation both lead to the development of this substantial
826 DO deficient zone. Note, that the magnitude and timescale of this decrease are broadly
827 consistent with observed low-oxygen events in the region, though specific rates from the model
828 should be interpreted cautiously.

829 The high PV water, that is advected from the west, acts as a barrier for the HBV and westward
830 propagation stops after day 300 (Fig. 10a and 10d). The HBV is deformed by the high PV
831 water, which likely leads to enhanced isopycnal and diapycnal mixing at the eddy periphery.
832 In fact, the HBV shrinks between days 300 and 400 as illustrated by the continuously
833 decreasing radius from 50 km to 30 km (Fig. 10b). Though, the core still shows source water
834 characteristics with unaltered low PV and low salinity, and still holds the DO deficient zone.
835 After day 400, the HBV starts to interact with surrounding water - partly being low in PV as well
836 - which weakens the isolation of the HBV core ($(U/c)^{-1} \approx 1$, Fig. 10f) and leads to continuous
837 increase of PV and DO. PV strongly increases after day 550 and reaches the PV threshold of
838 surrounding water at about day 600, where the core starts to dissolve as illustrated by the
839 strong increase of salinity and DO after day 600.

840 **5 Discussion**

841 Moored time series of dissolved oxygen (DO) in the near-equatorial Atlantic (4°N up to 12°N)
842 occasionally reveal pronounced drops in oxygen concentrations that fall significantly beneath
843 the climatological mean. These events occur well below the mixed layer and can persist for
844 several weeks. In addition, we found that about 8% of all observed CTD-O profiles in the near-
845 equatorial ETNA (25°-15°W, 6°-12°N) appear with anomalous low-DO (< 60 $\mu\text{mol kg}^{-1}$) in the
846 upper 200 m, which is as well below the climatological DO concentration. Until now, the causes
847 of these extreme low-DO events have remained unclear. Mesoscale eddies with low oxygen
848 cores - known to occur farther north around 20°N - are not expected to drive such extensive
849 oxygen-deficient zones in the near-equatorial region, as they are not believed to persist here
850 as coherent vortices with lifespans of several months or longer (Chaigneau et al., 2009;
851 Keppler et al., 2018). However, the majority of these low-DO events (60%) are clearly
852 associated with high-baroclinic subsurface-intensified eddies (Table 1, Fig. 4, Fig. 5). For the
853 remaining 40%, the velocity and density distributions did not reveal clear eddy signatures, nor
854 did satellite data - consistent with all identified vortices, which generally lack a distinct surface
855 signature. However, a connection to subsurface-intensified eddies cannot be ruled out a priori
856 for these cases.

857 This underlines that in understanding the Earth system, a better understanding of small-scale
858 ocean dynamics (smaller than the first baroclinic Rossby radius of deformation) is essential,
859 as they play a crucial role in the distribution of energy and tracers as well as the regulation of
860 biogeochemical processes. In particular, below the surface layer - where satellite observations
861 are ineffective - our understanding of the frequency, magnitude, and impact of these small-
862 scale ocean dynamics remains limited.

863 In the vicinity of the equator (< 5°N/S), mesoscale dynamics dominantly appear as horizontally
864 anisotropic waves (e.g. tropical instability waves) rather than closed circular structures. These
865 wave-like structures, however, are not isolated enough to effectively transport or develop low-
866 oxygen environments. The eddies with DO anomalies that we observed are relatively small
867 and long-lived high-baroclinic vortices (HBVs). Ship sections along 23°W exclusively revealed
868 anticyclonic HBVs, whereas both anticyclonic and cyclonic HBVs were found from moored
869 observations at 11°N/21°W and in the model.

870 **5.1 Vertical and horizontal structure of the low-oxygen events and the associated
871 high-baroclinic mode vortices**

872 The observed anticyclonic HBVs had a pronounced low-DO core that vertically extended from
873 the base of the mixed layer down to several hundred meter depth (with minimum DO at depths
874 between 45 and 90 m). The anomalous horizontal velocity of the observed anticyclonic HBVs
875 was at maximum (maximum EKE) at the depth of the DO minimum and extended from 50 to
876 roughly 250 m. Stratification in the observed anticyclonic HBVs' core was weak over this depth
877 range with upward and downward displaced isopycnals above and below the depth of EKE
878 maximum, respectively. We found an average radius of about 34 km (between 20 and 45 km)
879 for the observed HBVs. A decomposition into vertical baroclinic modes showed, that modes 4
880 to 10 fit best to low-DO events that are related to these HBVs. The associated 4th to 10th
881 baroclinic Rossby radii of deformation are between 34 and 13 km (at 9°N) and in good
882 agreement with the observed eddy radii. The observed radii appear well below the first
883 baroclinic Rossby radius of deformation (more than 100 km in the region) and corresponding
884 eddies can be considered as higher baroclinic mode vortices. Rossby numbers were below 1,
885 with values of approximately 0.3 - 0.7 estimated from shipboard observations (one eddy
886 crossing is shown in figure 6; others not shown) and around 0.1 - 0.4 in the GFDL CM2.6 model
887 simulation (exemplarily shown in Fig. 6 or Fig 10e).

888 The observed cyclonic HBVs appeared with a stratification maximum at about 150 m and a
889 cyclonic velocity structure with maximum EKE at a similar depth. Shallow DO minima were
890 found at 100 and 200 m throughout the transition, but without any clear separation from the

891 deep OMZ at 300 m. This less intensified DO minimum at 100 m and the missing intermediate
892 DO maximum at 200 m is a substantial difference to the DO distribution observed within
893 anticyclonic HBVs. However, enhanced DO consumption has been shown to be a reasonable
894 driver for DO depletion in a cyclonic HBV, that was observed in the western subtropical North
895 Atlantic (Li et al., 2008). Pure upwelling or upward mixing of low-DO water from the deep OMZ
896 cannot explain such vertically homogeneous distribution of low-DO between 100 and 300 m in
897 cyclonic HBVs. These processes would imply either a shallowing of isopycnal surfaces or a
898 weakened stratification within this depth range, which is contradictory to the observed
899 deepening of isopycnals above 150 m, shallowing of isopycnals below 150 m and
900 consequently the intensified stratification at 150 m (Fig. 5, Event #03). Due to the increased
901 stratification, the thickness of the intermediate DO maximum layer (that is associated with
902 isopycnal 26.6 kg m^{-3}) is reduced and very likely not resolved by the sparsely distributed
903 number of DO sensors.

904 We could not collocate any clear signals in SLA or SST from satellite observations with the in
905 situ observed HBVs. Shipboard observations showed a strongly weakening velocity signature
906 toward the surface. Also the simulated HBVs from GFDL CM2.6 model showed similar
907 characteristics as the observed vortices and no signature could be found from the surface
908 velocity. Moreover, the resolution and interpolation scheme for the gridded SLA data likely do
909 not allow to properly capture geostrophic structures at scales of smaller than about 40 km.
910 These are likely reasons, why near-equatorial subsurface eddies are hardly identified from
911 satellite products. If higher resolution satellite products from SWOT will allow to detect the
912 HBVs remains to be seen, though what we see from the in-situ observed structure and the
913 model results we conjecture that the high baroclinic mode HBVs tend to “hide” below the
914 surface/mixed layer base.

915 **5.2 Origin, lifetime & evolution of the oxygen content of high-baroclinic mode 916 vortices**

917 Water mass characteristics derived from shipboard observations showed that open ocean
918 water masses with DO below $60 \mu\text{mol kg}^{-1}$ in the upper 200 m (often associated with HBVs)
919 likely originate from the eastern boundary, where South Atlantic Central Water contributions
920 exceed those of North Atlantic Central Water. Model results are in agreement as they show
921 the formation of a low-DO HBVs with low PV in its core off the African coast at about
922 $10^\circ\text{N}/18^\circ\text{W}$. Hence, it is expected that the generation mechanism is consistent with previous
923 studies on HBV formation, in which the interaction between the mean flow and sharp
924 topographic curvature leads to the formation low-PV waters within the bottom boundary layer,
925 and the shedding of HBVs (D'Asaro, 1988; Molemaker et al., 2015; Thomsen et al., 2016;

926 Srinivasen et al., 2017; Dilmahamod et al., 2022).

927 The simulated HBV analyzed here propagated westward far into the open ocean over a
928 distance of 1,600 km (10°N/33°W) and lasted for 600 days (average propagation speed of
929 2.6 km day⁻¹). For the observed HBVs, we could not derive propagation speeds in a similar
930 way. Instead, we followed an approach by Nof (1981) and Rubino et al. (2009), who formulated
931 the westward translation of isolated high baroclinic eddies on a plane, which is given as a
932 function of the n -th baroclinic Rossby radius of deformation and the Rossby number:

$$C_n = -\frac{1}{3} \beta R_{d,n}^2 (1 - Ro)^{-1} \quad (2)$$

933 with β being the meridional derivative of the Coriolis parameter. Considering a Rossby radius
934 between 35 and 50 km and a Rossby number between 0.3 and 0.7 (taken as characteristic
935 scales from the observed HBVs corresponding to the vertical baroclinic mode 4) yields a
936 propagation speed between 1.1 and 5.4 km day⁻¹. This is in good agreement with the
937 propagation speed obtained from the simulated HBV. Considering the origin of the observed
938 low-DO HBVs at the eastern boundary (cf. section 4.4), a propagation speed at 1.1-5.4
939 km day⁻¹ yields a propagation time of 100 to 500 days to propagate a distance toward 23°W
940 (around 550 km). The fact, that these high baroclinic low-DO HBVs are not captured by satellite
941 products, prevents both backtracking to their origin and estimating their lifetime directly.

942 In contrast to anticyclonic HBVs, cyclonic HBVs were only detected twice in the mooring time
943 series and were not found in any of the numerous ship sections along 23°W. We may only
944 speculate, that cyclonic HBVs do not frequently propagate across 23°W due to a much more
945 reduced eddy life time. They transport anomalously high PV water in their core compared to
946 surrounding water masses. During westward propagation, the isolation of the core is expected
947 to be reduced due to the westward increasing PV background gradient in the tropical Atlantic.
948 As anticyclonic HBVs propagate westward, their low-PV cores are reinforced and remain
949 isolated from surrounding waters, promoting their longevity. However, encounters with high-
950 PV water from the western basin may destabilize them, while interactions with other low-PV
951 anticyclones can enhance their stability. During the lifetime of the simulated anticyclonic HBVs,
952 enhanced respiration within the eddy core contributes to a noticeable decrease in DO over
953 several months. While this trend is qualitatively consistent with observations of low-oxygen
954 events, the model-derived values should be considered indicative rather than quantitatively
955 precise. However, this fits to our observational results, where lowest absolute DO
956 concentrations occurred in the open ocean (24°-21°W) rather than in the region that is located
957 closer to the eastern boundary (21°-18°W). The DO consumption rates found here are also in
958 good agreement with consumption rates estimated from observed subsurface intensified

959 anticyclonic eddies ($0.19 \pm 0.08 \mu\text{mol kg}^{-1} \text{ d}^{-1}$) that originate from the Mauritanian upwelling
960 system and propagate westward at about 18°N (Schütte et al., 2016). We shall note, that DO
961 was observed close to anoxic conditions on the shelf of Senegal at about 14°N at depths of
962 about 20 m (Machu, 2019). However, these water masses are at much shallower depth and
963 lighter densities and are very likely not the source for the low-DO core of the here described
964 offshore HBVs. However, the low-DO eddies described here, characterized with low PV waters
965 in their cores, likely have their origin at the eastern boundary with the bottom boundary layer
966 identified as the source of this low PV waters.

967 **6 Summary and conclusion**

968 We shall summarize the following take home messages to the reader:

969 (i) Distribution and occurrence of low-DO events:

970 In the near-equatorial North Atlantic (25° - 15°W , 6° - 12°N), about 8% of all CTD-O
971 profiles occur with a DO concentration of less than $60 \mu\text{mol kg}^{-1}$ in the upper 200 m,
972 which is well below the climatological DO concentration. These extreme low-DO
973 events are more frequent and more intensified in the open ocean (30° - 21°W)
974 compared to the region east of it (21° - coast of West Africa). Unprecedented low-
975 DO concentrations were found with $1 \mu\text{mol kg}^{-1}$ at 80 m depth at the mooring
976 located at $11^\circ\text{N}/23^\circ\text{W}$ as well as $17 \mu\text{mol kg}^{-1}$ ($8^\circ\text{N}/23^\circ\text{W}$) and $29 \mu\text{mol kg}^{-1}$
977 ($9^\circ\text{N}/21^\circ\text{W}$) observed with ship based measurements.

978 (ii) Low-DO events are related to subsurface intensified submesoscale coherent vortices:

979 We found 66% of open ocean low-DO events to be related to subsurface-intensified
980 submesoscale coherent vortices, with anticyclonic eddies appearing to dominate.
981 The vertical structure of these vortices is characterized by high baroclinic modes
982 (modes 4 to 10), and they are confined to the upper 250 m. In situ velocity
983 observations revealed an average radius of 34 km, which is well below the first
984 baroclinic Rossby radius of deformation ($O(100 \text{ km})$), but agrees well with Rossby
985 radii of the higher baroclinic modes 4 to 10 (34 to 13 km at 9°N). Despite the small
986 length scales, the Rossby number of the vortices is below 1, assigning them to the
987 dynamical range of mesoscale variability.

988 (iii) Origin and life time:

989 The vortices most likely originate from the eastern boundary. They can propagate
990 far into the open ocean with a propagation speed of 1.8 - 4.9 km day^{-1} , reaching a
991 life time of more than half a year (it took around 100 to 500 days to propagate the
992 550 km distance towards 23°W). This is much longer than currently considered
993 possible, given the highly dynamical area and the proximity to the equator. Model

994 simulations even show a life time of up to 1.5 years. Cyclonic eddies with low-
995 oxygen cores were less frequent than anticyclonic eddies. Cyclonic eddies were
996 not found in ship sections along 23°W, but in the minority of all low-DO extreme
997 events from moored observations at 11°N/21°W.

998 (iv) Impact of the vortices on DO and biogeochemistry:

999 Near-equatorial anticyclonic vortices have unexpectedly long lifetimes and strongly
1000 isolate their low-PV cores from surrounding water. This can create a DO deficient
1001 zone, due to enhanced primary production on top and remineralization (DO
1002 decrease of $0.16 \mu\text{mol kg}^{-1} \text{ day}^{-1}$ for the simulated anticyclonic vortices),
1003 accompanied by elevated nitrate levels in the eddy core.

1004 (v) Detection of near-equatorial vortices with remote sensing satellites:

1005 Near-equatorial vortices are hardly detectable by conventional satellite altimetry
1006 observations, which precludes a backtracking of these eddies. New observations
1007 are desirable to verify whether the new SWOT mission can capture such HBV,
1008 although a strong surface signal is not expected due to the mainly subsurface
1009 structure (also supported by the model).

1010 Subsurface coherent vortices in the near-equatorial ocean have been so far overlooked in
1011 driving DO deficient zones. The long-lived vortices appear unexpectedly quite regularly given
1012 theoretical considerations and are able to generate hypoxic regimes in the open ocean, which
1013 may have localized effects habitats, biodiversity and biogeochemical cycling. They are typically
1014 not tracable in satellite products, which makes a collocation of satellite data with in-situ
1015 observations (CTD-O, Argo profiles, moored observations) hardly possible. The comparatively
1016 coarse resolution of satellite observations might instead lead to a wrong collocation of the
1017 subsurface low-DO events with larger surface intensified mesoscale structures nearby. The
1018 mechanisms for the generation of these near-equatorial low-DO eddies remain an open
1019 question. So far, we here identified a potential source region and provided a first insight about
1020 the dynamics (life time, baroclinicity, isolation) of these eddies. A more comprehensive
1021 investigation from high resolution ocean circulation models - coupled to biogeochemistry -
1022 would shed light onto the generation. Further, the study of the temporal evolution of dominant
1023 vertical baroclinic modes throughout the eddies' life cycle would contribute to a better
1024 understanding of the eddy dynamics and stability. Moreover, the interdisciplinary view on
1025 changes in biogeochemical processes would increase the understanding about the impact on
1026 biogeochemistry. The in-situ tracking and observation of these eddies over their life cycle is
1027 challenging, but would provide key information to validate the simulation of these eddies.

1029 **7 Data availability**

1030 The assembled shipboard measurements (27 research cruises) and moored data used in this
1031 paper are available and collected at <https://doi.pangaea.de/10.1594/PANGAEA.987397>. The
1032 used satellite altimetry data is provided by Marine Copernicus (<https://marine.copernicus.eu>)
1033 can be downloaded at <https://doi.org/10.48670/moi-00148>. The used gridded climatological
1034 hydrography and oxygen from the World Ocean Atlas 2023 (WOA23), is available at NOAA
1035 under: <https://doi.org/10.25921/va26-hv25>. The Model data will be made openly accessible via
1036 the GEOMAR website <https://data.geomar.de> where data is uniquely identifiable via handle
1037 assignment (PID) and will be accessible per download.

1038 **Author contributions**

1039 Conceptualization: FS, JH, PB, Data curation: JH, IF, FS, Formal analysis and methodology:
1040 JH, IF, MS, FS, AB, AFD, Funding acquisition: PB, FS, JH Writing – original draft: JH, FS, IF,
1041 Writing – review and editing: FS, JH, IF, AB, AFD, MS, PB

1042

1043 **Competing interests**

1044 The contact author has declared that none of the authors has any competing interests.

1045

1046 **Acknowledgements**

1047 We thank the scientific crews and the “Leitstelle Deutsche Forschungsschiffe” for supporting the
1048 numerous expeditions in the eastern tropical North Atlantic that have made this work possible.
1049 Research cruises with RV Meteor and RV Maria S. Merian were funded by the Deutsche
1050 Forschungsgemeinschaft as part of Sonderforschungsbereich 754 “Climate-Biogeochemistry
1051 Interactions in the Tropical Ocean” and by EU H2020 under grant agreement number 817578
1052 (TRIATLAS) and grant agreement number 101136548 (ObsSea4Clim). Moored velocity and oxygen
1053 observations were partly acquired in cooperation with the PIRATA project, and we would like to thank
1054 B. Bourlès, R. Lumpkin, C. Schmid, and G. Foltz for their help with mooring work and data sharing. We
1055 thank the captains and crew of the RV *Maria S. Merian*, RV *Meteor*, RV *Poseidon*, and RV *L’Atalante* as
1056 well as our technical group for their help with the fieldwork.

References

Antonov, J. I., Seidov, D., Boyer, T. P., Locarnini, R. A., Mishonov, A. V., Garcia, H. E., Baranova, O. K., Zweng, M. M., and Johnson, D. R.: *World Ocean Atlas 2009, Volume 2: Salinity*. S. Levitus, Ed. NOAA Atlas NESDIS 69, U.S. Government Printing Office, Washington, D.C., 184 pp, 2010.

Bendinger, A., Dilmahamod, A. F., Albert, A., Le Sommer, J., and Karstensen, J.: Characteristics of Mesoscale-to-Submesoscale Eddies in the Labrador Sea: Insights from Ship Observations. *J. Phys. Oceanogr.*, 55, 2037–2057, <https://doi.org/10.1175/JPO-D-24-0216.1>, 2025.

Bittig, H. C., Körtzinger, A., Neill, C., van Ooijen, E., Plant, J. N., Hahn, J., Johnson, K. S., Yang, B., and Emerson, S. R.: Oxygen Optode Sensors: Principle, Characterization, Calibration, and Application in the Ocean, *Frontiers in Marine Science*, 4, 10.3389/fmars.2017.00429, 2018.

Brandt, P., Hormann, V., Körtzinger, A., Visbeck, M., Krahmann, G., Stramma, L., Lumpkin, R., and Schmid, C.: Changes in the Ventilation of the Oxygen Minimum Zone of the Tropical North Atlantic, *J. Phys. Oceanogr.*, 40, 1784-1801, 10.1175/2010jpo4301.1, 2010.

Brandt, P., Bange, H. W., Banyte, D., Dengler, M., Didwischus, S. H., Fischer, T., Greatbatch, R. J., Hahn, J., Kanzow, T., Karstensen, J., Körtzinger, A., Krahmann, G., Schmidtko, S., Stramma, L., Tanhua, T., and Visbeck, M.: On the role of circulation and mixing in the ventilation of oxygen minimum zones with a focus on the eastern tropical North Atlantic, *Biogeosciences*, 12, 489-512, 10.5194/bg-12-489-2015, 2015.

Calil, P. H. R.: High-Resolution, Basin-Scale Simulations Reveal the Impact of Intermediate Zonal Jets on the Atlantic Oxygen Minimum Zones. *Journal of Advances in Modeling Earth Systems*, 15(2), e2022MS003158.
<https://agupubs.onlinelibrary.wiley.com/doi/abs/10.1029/2022MS003158>, 2023

Castelão, G. P., and W. E. Johns (2011), Sea surface structure of North Brazil Current rings derived from shipboard and moored acoustic Doppler current profiler observations, *J. Geophys. Res.*, 116, C01010, doi:10.1029/2010JC006575.

Castelão, G. P., Irber, L. C., & Villas Boas, A. B. M. (2013). An objective reference system for studying rings in the ocean. *Computers & geosciences*, 61, 43-49.
<https://www.sciencedirect.com/science/article/pii/S0098300413001933>

Chaigneau, A., Eldin, G., and Dewitte, B.: Eddy activity in the four major upwelling systems from satellite altimetry (1992-2007), *Prog. Oceanogr.*, 83, 117-123, 10.1016/j.pocean.2009.07.012, 2009.

Chelton, D. B., deSzoeke, R. A., Schlax, M. G., Naggar, K. E., and Siwertz, N.: Geographical Variability of the First Baroclinic Rossby Radius of Deformation, *J. Phys. Oceanogr.*, 28, 433-460, 10.1175/1520-0485(1998)028<0433:Gvotfb>2.0.Co;2, 1998.

Chelton, D. B., Schlax, M. G., and Samelson, R. M.: Global observations of nonlinear mesoscale eddies, *Prog. Oceanogr.*, 91, 167-216, 10.1016/j.pocean.2011.01.002, 2011.

Christiansen, S., Hoving, H. J., Schutte, F., Hauss, H., Karstensen, J., Kortzinger, A., Schroder, S. M., Stemmann, L., Christiansen, B., Picheral, M., Brandt, P., Robison, B., Koch, R., and Kiko, R.: Particulate matter flux interception in oceanic mesoscale eddies by the polychaete *Poeobius* sp, *Limnol. Oceanogr.*, 63, 2093-2109, 10.1002/lno.10926, 2018.

D'Asaro, E. A.: Generation of submesoscale vortices: A new mechanism, *Journal of Geophysical Research: Oceans*, 93, 6685-6693, 10.1029/JC093iC06p06685, 1988.

Delworth, T. L., Rosati, A., Anderson, W., Adcroft, A. J., Balaji, V., Benson, R., Dixon, K., Griffies, S. M., Lee, H.-C., Pacanowski, R. C., Vecchi, G. A., Wittenberg, A. T., Zeng, F., and Zhang, R.: Simulated Climate and Climate Change in the GFDL CM2.5 High-Resolution Coupled Climate Model, *J. Clim.*, 25, 2755-2781, 10.1175/jcli-d-11-00316.1, 2012.

Dilmahamod, A. F., J. Karstensen, H. Dietze, U. Löptien, and K. Fennel, 2022: Generation Mechanisms of Mesoscale Eddies in the Mauritanian Upwelling Region. *J. Phys. Oceanogr.*, 52, 161–182, <https://doi.org/10.1175/JPO-D-21-0092.1>.

Deutsch, C., Penn, J.L. & Seibel, B. Metabolic trait diversity shapes marine biogeography. *Nature* 585, 557–562 (2020). <https://doi.org/10.1038/s41586-020-2721-y>

Dufour, C. O., Griffies, S. M., de Souza, G. F., Frenger, I., Morrison, A. K., Palter, J. B., Sarmiento, J. L., Galbraith, E. D., Dunne, J. P., Anderson, W. G., and Slater, R. D.: Role of Mesoscale Eddies in Cross-Frontal Transport of Heat and Biogeochemical Tracers in the Southern Ocean, *J. Phys. Oceanogr.*, 45, 3057-3081, 10.1175/jpo-d-14-0240.1, 2015.

Duteil, O., Schwarzkopf, F. U., Böning, C. W., and Oschlies, A.: Major role of the equatorial current system in setting oxygen levels in the eastern tropical Atlantic Ocean: A high-resolution model study, *Geophys. Res. Lett.*, 41, 2033-2040, 10.1002/2013gl058888, 2014.

Eden, C.: Eddy length scales in the North Atlantic Ocean, *J. Geophys. Res.-Oceans*, 112, 10.1029/2006jc003901, 2007.

Fiedler, B., Grundle, D. S., Schütte, F., Karstensen, J., Löscher, C. R., Hauss, H., Wagner, H., Loginova, A., Kiko, R., Silva, P., Tanhua, T., and Körtzinger, A.: Oxygen utilization and downward carbon flux in an oxygen-depleted eddy in the eastern tropical North Atlantic, *Biogeosciences*, 13, 5633-5647, 10.5194/bg-13-5633-2016, 2016.

Fischer, J., Brandt, P., Dengler, M., Müller, M., and Symonds, D.: Surveying the Upper Ocean with the Ocean Surveyor: A New Phased Array Doppler Current Profiler, *J. Atmos. Ocean. Technol.*, 20, 742-751, 10.1175/1520-0426(2003)20<742:Stuwt>2.0.Co;2, 2003.

Frenger, I., Bianchi, D., Stührenberg, C., Oschlies, A., Dunne, J., Deutsch, C., Galbraith, E., and Schütte, F.: Biogeochemical Role of Subsurface Coherent Eddies in the Ocean: Tracer Cannonballs, Hypoxic Storms, and Microbial Stewpots?, *Glob. Biogeochem. Cycle*, 32, 226-249, doi:10.1002/2017GB005743, 2018.

Galbraith, E. D., Dunne, J. P., Gnanadesikan, A., Slater, R. D., Sarmiento, J. L., Dufour, C. O., de Souza, G. F., Bianchi, D., Claret, M., Rodgers, K. B., and Marvasti, S. S.: Complex functionality with minimal computation: Promise and pitfalls of reduced-tracer ocean biogeochemistry models, *Journal of Advances in Modeling Earth Systems*, 7, 2012-2028, 10.1002/2015ms000463, 2015.

Garcia, H. E., Locarnini, R. A., Boyer, T. P., Antonov, J. I., Baranova, O. K., Zweng, M. M., and Johnson, D. R.: *World Ocean Atlas 2009, Volume 3: Dissolved Oxygen, Apparent Oxygen Utilization, and Oxygen Saturation*. S. Levitus, Ed. NOAA Atlas NESDIS 70, U.S. Government Printing Office, Washington, D.C., 344 pp, 2010a.

Garcia, H. E., Locarnini, R. A., Boyer, T. P., Antonov, J. I., Zweng, M. M., Baranova, O. K., and Johnson, D. R.: *World Ocean Atlas 2009, Volume 4: Nutrients (phosphate, nitrate, silicate)*. S. Levitus, Ed. NOAA Atlas NESDIS 71, U.S. Government Printing Office, Washington, D.C., 398 pp., 2010b.

Gill, A. E.: *Atmosphere-Ocean Dynamics*, International Geophysics Series Volume 30, Academic Press, New York, 1982.

Griffies, S. M., Winton, M., Anderson, W. G., Benson, R., Delworth, T. L., Dufour, C. O., Dunne, J. P., Goddard, P., Morrison, A. K., Rosati, A., Wittenberg, A. T., Yin, J., and Zhang, R.: Impacts on Ocean Heat from Transient Mesoscale Eddies in a Hierarchy of Climate Models, *J. Clim.*, 28, 952-977, 10.1175/jcli-d-14-00353.1, 2015.

Gula, J., Blacic, T. M., and Todd, R. E.: Submesoscale Coherent Vortices in the Gulf Stream, *Geophys. Res. Lett.*, 46, 2704-2714, 10.1029/2019gl081919, 2019.

Hahn, J., Brandt, P., Greatbatch, R. J., Krahmann, G., and Körtzinger, A.: Oxygen variance and meridional oxygen supply in the Tropical North East Atlantic oxygen minimum zone, *Clim. Dyn.*, 43, 2999-3024, 10.1007/s00382-014-2065-0, 2014.

Hahn, J., Brandt, P., Schmidtko, S., and Krahmann, G.: Decadal oxygen change in the eastern tropical North Atlantic, *Ocean Science*, 13, 551-576, 10.5194/os-13-551-2017, 2017.

Hauss, H., Christiansen, S., Schutte, F., Kiko, R., Lima, M. E., Rodrigues, E., Karstensen, J., Loscher, C. R., Körtzinger, A., and Fiedler, B.: Dead zone or oasis in the open ocean? Zooplankton distribution and migration in low-oxygen modewater eddies, *Biogeosciences*, 13, 1977-1989, 10.5194/bg-13-1977-2016, 2016.

Karstensen, J., Stramma, L., and Visbeck, M.: Oxygen minimum zones in the eastern tropical Atlantic and Pacific oceans, *Prog. Oceanogr.*, 77, 331-350, 10.1016/j.pocean.2007.05.009, 2008.

Karstensen, J., Fiedler, B., Schütte, F., Brandt, P., Körtzinger, A., Fischer, G., Zantopp, R., Hahn, J., Visbeck, M., and Wallace, D.: Open ocean dead zones in the tropical North Atlantic Ocean, *Biogeosciences*, 12, 2597-2605, 10.5194/bg-12-2597-2015, 2015.

Karstensen, J., Schütte, F., Pietri, A., Krahmann, G., Fiedler, B., Grundle, D., Hauss, H., Körtzinger, A., Loscher, C. R., Testor, P., Vieira, N., and Visbeck, M.: Upwelling and isolation in oxygen-depleted anticyclonic modewater eddies and implications for nitrate cycling, *Biogeosciences*, 14, 2167-2181, 10.5194/bg-14-2167-2017, 2017.

Keppler, L., Cravatte, S., Chaigneau, A., Pegliasco, C., Gourdeau, L., and Singh, A.: Observed Characteristics and Vertical Structure of Mesoscale Eddies in the Southwest Tropical Pacific, *Journal of Geophysical Research: Oceans*, 123, 2731-2756, 10.1002/2017jc013712, 2018.

Key, R. M., Kozyr, A., Sabine, C. L., Lee, K., Wanninkhof, R., Bullister, J. L., Feely, R. A., Millero, F. J., Mordy, C., and Peng, T.-H.: A global ocean carbon climatology: Results from Global Data Analysis Project (GLODAP), *Glob. Biogeochem. Cycle*, 18, 10.1029/2004gb002247, 2004.

Köhn, E. E., Greatbatch, R. J., Brandt, P., and Claus, M.: The formation and ventilation of an oxygen minimum zone in a simple model for latitudinally alternating zonal jets, *Ocean Sci.*, 20, 1281–1290, <https://doi.org/10.5194/os-20-1281-2024>, 2024.

Li, Q. P., Hansell, D. A., McGillicuddy Jr., D. J., Bates, N. R., and Johnson, R. J.: Tracer-based assessment of the origin and biogeochemical transformation of a cyclonic eddy in the Sargasso Sea, *Journal of Geophysical Research: Oceans*, 113, 10.1029/2008jc004840, 2008.

Locarnini, R. A., Mishonov, A. V., Antonov, J. I., Boyer, T. P., Garcia, H. E., Baranova, O. K., Zweng, M. M., and Johnson, D. R.: *World Ocean Atlas 2009, Volume 1: Temperature*. S.

Levitus, Ed. NOAA Atlas NESDIS 68, U.S. Government Printing Office, Washington, D.C., 184 pp, 2010.

Löscher, C. R., Fischer, M. A., Neulinger, S. C., Fiedler, B., Philippi, M., Schütte, F., Singh, A., Hauss, H., Karstensen, J., Kötzinger, A., Künzel, S., and Schmitz, R. A.: Hidden biosphere in an oxygen-deficient Atlantic open-ocean eddy: future implications of ocean deoxygenation on primary production in the eastern tropical North Atlantic, *Biogeosciences*, 12, 7467-7482, 10.5194/bg-12-7467-2015, 2015.

Machu, E., Capet, X., Estrade, P. A., Ndoye, S., Brajard, J., Baurand, F., Auger, P.-A., Lazar, A., and Brehmer, P.: First Evidence of Anoxia and Nitrogen Loss in the Southern Canary Upwelling System, *Geophys. Res. Lett.*, 46, 2619-2627, 10.1029/2018gl079622, 2019.

McCoy, D., Bianchi, D., and Stewart, A. L.: Global observations of submesoscale coherent vortices in the ocean, *Prog. Oceanogr.*, 189, 102452, <https://doi.org/10.1016/j.pocean.2020.102452>, 2020.

McGillicuddy, D. J.: Formation of Intrathermocline Lenses by Eddy-Wind Interaction, *J. Phys. Oceanogr.*, 45, 606-612, 10.1175/jpo-d-14-0221.1, 2015.

McGillicuddy, D. J.: Mechanisms of Physical-Biological-Biogeochemical Interaction at the Oceanic Mesoscale, in: *Annual Review of Marine Science*, Vol 8, edited by: Carlson, C. A., and Giovannoni, S. J., *Annual Review of Marine Science*, Annual Reviews, Palo Alto, 125-+, 2016.

McWilliams, J. C.: Submesoscale, coherent vortices in the ocean, *Reviews of Geophysics*, 23, 165-182, 10.1029/RG023i002p00165, 1985.

Molemaker, M. J., McWilliams, J. C., and Dewar, W. K.: Submesoscale Instability and Generation of Mesoscale Anticyclones near a Separation of the California Undercurrent, *J. Phys. Oceanogr.*, 45, 613-629, 10.1175/jpo-d-13-0225.1, 2015.

Nof, D.: On the β -Induced Movement of Isolated Baroclinic Eddies, *J. Phys. Oceanogr.*, 11, 1662-1672, 10.1175/1520-0485(1981)011<1662:Otimo>2.0.Co;2, 1981.

Peña-Izquierdo, J., van Sebille, E., Pelegrí, J. L., Sprintall, J., Mason, E., Llanillo, P. J., & Machín, F. (2015). Water mass pathways to the North Atlantic oxygen minimum zone. *Journal of Geophysical Research: Oceans*.

Philander, S. G. H.: Forced oceanic waves, *Reviews of Geophysics*, 16, 15-46, 10.1029/RG016i001p00015, 1978.

Reagan, James R.; Boyer, Tim P.; García, Hernán E.; Locarnini, Ricardo A.; Baranova, Olga K.; Bouchard, Courtney; Cross, Scott L.; Mishonov, Alexey V.; Paver, Christopher R.; Seidov, Dan; Wang, Zhankun; Dukhovskoy, Dmitry: *World Ocean Atlas 2023*. NOAA National Centers for Environmental Information, 2024

Rubino, A., Dotsenko, S., and Brandt, P.: Nonstationary Westward Translation of Nonlinear Frontal Warm-Core Eddies, *J. Phys. Oceanogr.*, 39, 1486-1494, 10.1175/2008jpo4089.1, 2009.

Schütte, F., Brandt, P., & Karstensen, J. (2016a). Occurrence and characteristics of mesoscale eddies in the tropical northeastern Atlantic Ocean. *Ocean Sci.*, 12(3), 663-685. <https://www.ocean-sci.net/12/663/2016/>, 2016

Schütte, F., Karstensen, J., Krahmann, G., Hauss, H., Fiedler, B., Brandt, P., Visbeck, M., and Körtzinger, A.: Characterization of "dead-zone" eddies in the eastern tropical North Atlantic, *Biogeosciences*, 13, 5865-5881, 10.5194/bg-13-5865-2016, 2016b.

Shcherbina, A. Y., Rudnick, D. L., and Talley, L. D.: Ice-draft profiling from bottom-mounted ADCP data, *J. Atmos. Ocean. Technol.*, 22, 1249-1266, 10.1175/jtech1776.1, 2005.

Stramma, L., Bange, H. W., Czeschel, R., Lorenzo, A., and Frank, M.: On the role of mesoscale eddies for the biological productivity and biogeochemistry in the eastern tropical Pacific Ocean off Peru, *Biogeosciences*, 10, 7293-7306, 10.5194/bg-10-7293-2013, 2013.

R. Srinivasan, V. Rajendran, Shijo Zacharia, Tata Sudhakar, M.A. Atmanand: Indigenized Indian Drifting Buoys with INSAT Communication for Ocean Observations, *Ocean Engineering*, Volume 145, 2017, <https://doi.org/10.1016/j.oceaneng.2017.08.054>.

Thomsen, S., Kanzow, T., Krahmann, G., Greatbatch, R. J., Dengler, M., and Lavik, G.: The formation of a subsurface anticyclonic eddy in the Peru-Chile Undercurrent and its impact on the near-coastal salinity, oxygen, and nutrient distributions, *Journal of Geophysical Research: Oceans*, 121, 476-501, doi:10.1002/2015JC010878, 2016.

van Leeuwen, P. J.: The Propagation Mechanism of a Vortex on the β Plane, *J. Phys. Oceanogr.*, 37, 2316-2330, 10.1175/jpo3107.1, 2007.

Vic, C., B. Ferron, V. Thierry, H. Mercier, and P. Lherminier, 2021: Tidal and Near-Inertial Internal Waves over the Reykjanes Ridge. *J. Phys. Oceanogr.*, 51, 419-437, <https://doi.org/10.1175/JPO-D-20-0097.1>.

Vic, C., & Ferron, B. (2023). Observed structure of an internal tide beam over the Mid-Atlantic Ridge. *Journal of Geophysical Research: Oceans*, 128, e2022JC019509. <https://doi.org/10.1029/2022JC019509>

Visbeck, M.: Deep velocity profiling using lowered acoustic Doppler current profilers: Bottom track and inverse solutions, *J. Atmos. Ocean. Technol.*, 19, 794-807, 10.1175/1520-0426(2002)019<0794:dvpula>2.0.co;2, 2002.

Table 1. Low-DO events (below 60 $\mu\text{mol kg}^{-1}$) found in the upper 200 m during meridional CTD-O ship sections along 23°W between 7° and 12°N. Only those low-DO events are listed, where meridional sections of DO, hydrography and velocity were available (spanning a latitude range of minimum 3°). Columns from left to right denote DO minimum between 0 and 200 m, corresponding depth, latitude and research cruise with date of the CTD-O profile. The last three columns denote type, core position and radius of related eddy, that was analyzed with the eddy identification method. ACE events are marked in bold (the abbreviation ACME stands for anticyclonic mode water eddy). As an example, the event in the third row (Meteor 119/1, 17-Sep-2015) is presented in Fig. 4.

DO minimum [$\mu\text{mol kg}^{-1}$]	Depth [m]	Latitude [°N]	Cruise ID (Date)	Eddy type	Eddy core position	Radius [km]
17	59	8,0	Meteor 116/1 (22-May-2015)	ACME	8.3 °N 23.1 °W	33
37	63	11,5	Meteor 116/1 (21-May-2015)	-	-	-
42	71	8,0	Meteor 119/1 (17-Sep-2015)	ACME	8.0 °N 23.3 °W	38
44	45	10,0	Ronald H. Brown PNE09 (24-Jul-2009)	ACME	10.3 °N 23.2 °W	36
47	69	10,5	Polarstern PS88.2 (08-Nov-2014)	ACE	10.3 °N 23.2 °W	37
48	77	11,5	Ronald H. Brown PNE09 (24-Jul-2009)	ACME	11.6 °N 22.9 °W	31
52	75	11,5	L'Atalante IFM-GEOMAR 4 (11-Mar-2008)	-	-	-
53	67	11,0	Meteor 097/1 (30-May-2013)	-	-	-
54	93	7,0	Meteor 068/2 (04-Jul-2006)	ACME	7.1 °N 23.0 °W	20
55	65	10,5	Merian 018/3 (25-Jun-2011)	-	-	-
56	74	7,0	Ronald H. Brown PNE06 (30-Jun-2006)	ACME	7.0 °N 23.0 °W	45
57	71	11,5	Meteor 130/1 (03-Sep-2016)	-	-	-
58	82	11,0	Meteor 105/1 (10-Apr-2014)	ACME	11.0 °N 23.2 °W	60
58	73	11,5	Merian 022/1 (15-Nov-2012)	ACME	11.6 °N 23.0 °W	37
58	79	10,5	Meteor 106/1 (24-Apr-2014)	ACME	10.4 °N 23.2 °W	33